Supplementary Information

Hexaazaphenalene-directed pore-space-partitioned metal-organic frameworks for enhanced CO_2 capture and photocatalytic fixation

Zi-Yuan Liu, Shu-Cong Fan, Jia-Wen Wang, Li-Qiu Yang, Chen-Chen Xing, Wen-Yu Yuan, Ying Wang, Shun-Fu Du, Quan-Guo Zhai*

Key Laboratory of Applied Surface and Colloid Chemistry, Ministry of Education, Key Laboratory of Macromolecular Science of Shaanxi Province, School of Chemistry & Chemical Engineering, Shaanxi Normal University, Xi'an, Shaanxi, China

*Corresponding author,
zhaiqg@snnu.edu.cn (Quan-Guo Zhai)

General Methods and Materials.

Powder X-ray diffraction (PXRD) patterns were tested by a MiniFlex 600 X-ray diffractometer with Cu-Kα (λ =1.5406 Å) radiation in the 2θ range of 5-50°. Energy dispersive spectroscopy (EDS) and elemental mappings of MOFs were analyzed by an environmental scanning electron microscope (FEI, Quanta 200). Thermogravimetric analyses (TGA) were recorded on a thermal analyzer (Hengjiu, HCT-1) under an N_2 atmosphere in the range of 25-500 °C. UV-Vis-NIR spectrophotometer (Perkin-Elmer, Lambd 1050) was used to analyze the light absorption and $BaSO_4$ was used as the substrate. XPS valence band spectra were tested with an X-ray Photoelectron Spectroscopy (Escalab Xi+, Thermo Scientific). The CO_2 temperature programmed desorption (CO_2-TPD) curves were conducted on an AutoChem II 2920VG catalytic characterization system. In situ FT-IR experiments were tested with a Nicolet™ iS50 FTIR spectrometer. The band gaps of SNNU-384-385 MOFs were calculated according to the Tauc plot by linear extrapolation based on UV–vis diffuse reflectance spectroscopy.

Synthesis of SNNU-384-Co.

A mixed solution containing $CoSO_4 \cdot 7H_2O$ (58 mg, 0.2 mmol), [1,1'-biphenyl]-3,4',5-tricarboxylic acid (H_3BPTC, 29 mg, 0.1 mmol), 2,5,8-tri(4-pyridyl)-1,3,4,6,7,9-hexaazaphenalene (TPHAP, 20 mg, 0.05 mmol), N,N-dimethylacetamide (DMA, 4 mL), and methanol (1 mL) was placed in a 25 mL glass vial and stirred for 30 min to form a homogeneous solution. The mixture was then sealed and heated at 120 °C for 3 days. The product was washed with DMA/CH_3CN, yielding pure red icosahedral crystals with a 46% yield (based on Co).

Single Crystal X-ray Diffraction.

The single-crystal structure was performed on a Bruker D8 Venture diffractometer with graphite-monochromatic Cu-Kα radiation (λ = 1.541785 Å). The crystal structure was analyzed and refined by Olex2 software. The disordered solvent molecules were removed by the Solvent Mask in Olex2. Crystal data as well as details of data collection and refinements were summarized in Tables S1.

Calculation of Framework Charge for SNNU-384 and SNNU-385.

The electrical neutrality of two MOF frameworks was rigorously calculated and verified based on refined single-crystal X-ray diffraction data, definite ligand protonation states, intrinsic metal ion charges and the presence of coordinated water molecules, with the detailed charge balance calculations as follows:

1. SNNU-384 [$Ni_3(BPTC)_2(TPHAP)_2(H_2O)$].

Metal ion charge contribution: The framework contains three Ni^{2+} metal ions, with a total positive charge of + 6 ($3 \times Ni^{2+} = 6$).

Ligand charge contribution: The deprotonated anionic linker is $BPTC^{3-}$, with two $BPTC^{3-}$ ligands contributing a total negative charge of -6 ($2 \times BPTC^{3-} = 2 \times -3 = -6$); the TPHAP ligand is neutral (0 charge) and no net charge is contributed.

Coordinated water: The coordinated water molecule (H_2O) is neutral (0 charge) and no net charge is contributed.

Total charge balance: +6 (metal ions) + (-6) (anionic ligands) + 0 (TPHAP) + 0 (coordinated water) = 0.

The total charge of the SNNU-384 framework is zero, confirming its electrical neutrality.

2. SNNU-385 [$Ni_3(BPDB)_3(TPHAP)$].

Metal ion charge contribution: The framework contains three Ni^{2+} metal ions, with a total positive charge of +6 ($3 \times Ni^{2+} = 3 \times +2 = +6$).

Ligand charge contribution: The deprotonated anionic linker is $BPDB^{2-}$, with three $BPDB^{2-}$ ligands contributing a total negative charge of -6 ($3 \times BPDB^{2-} = 3 \times -2 = -6$); the TPHAP ligand is neutral (0 charge) and no net charge is contributed.

Total charge balance: +6 (metal ions) + (-6) (anionic ligands) + 0 (TPHAP) = 0.

The total charge of the SNNU-385 framework is zero, confirming its electrical neutrality.

Photoelectrochemical measurements

EIS and photocurrent experiments were tested using a CHI 760e electrochemical workstation. 0.1 M Tetrabutylammonium hexafluorophosphate ($TBAPF_6$) was used as the electrolyte, Ag/Ag^+ as the reference electrode, a platinum sheet as the counter electrode and conductive glass as the working electrode. 10 mg sample was ground and dispersed in a solution

containing 950 μL isopropanol and 50 μL naphthol, and 100 μL of the suspension was added dropwise on a conductive glass (1×1 cm^2) and dried at room temperature to prepare the working electrode.

Gas Adsorption Experiments.

Degassed MOF samples (60−120 mg) were used for gas adsorption-desorption experiments. CO_2 and N_2 adsorption isotherms on SNNU-384-385 MOFs were carried out on a Micromeritics ASAP 2020 HD88 surface-area and pore-size analyzer up to 1 atm of gas pressure by the static volumetric method. All used gases were of 99.999% purity. The temperature of 77 K was controlled by liquid nitrogen and other temperatures were controlled by a circulating bath of ethanol/H_2O.

Isosteric Heat of Adsorption.

To extract the coverage-dependent isosteric heat of adsorption, the data were modeled with a virial-type expression composed of the temperature-independent parameters a_i and b_i. The data were fitted using the equation:

$$ln\,P = ln\,N + \frac{1}{T}\sum_{i=0}^{m} a_i N_i + \sum_{i=0}^{n} b_i N_i \qquad \text{(eq. 1)}$$

where P is pressure expressed in Pa, N is the amount adsorbed in mmol g^{-1}, T is the temperature in K, m and n determine the number of terms required to adequately describe the isotherm, and ai and bi are virial coefficients. The values of the virial coefficients a0 through am were then used to calculate the isosteric heat of absorption using the following equation:

$$Q_{st} = -R\sum_{i=0}^{m} a_i N^i \qquad \text{(eq. 2)}$$

where Q_{st} (kJ mol^{-1}) is the isosteric heat of adsorption at a specific surface loading of adsorbate, R (kJ·mol^{-1} K^{-1}) is the universal gas constant. The coverage dependencies of Q_{st} calculated from fitting the 273 and 298 K (under the pressure range from 0−1 bar) data are presented in Table S10-11 for SNNU-384 and SNNU-385 MOFs.

CO_2 Cycloaddition Experiments.

A certain amount of epoxide and catalyst was placed in a stainless-steel reaction vessel without solvent and cocatalyst. Before the reaction, the CO_2 gas (1 bar) was bubbled into the mixture for 15 min to remove air. Then the reactor was irradiated by a 300 W Xe lamp (λ>420 nm). After the reaction, the reaction mixture was extracted using acetonitrile (CH_3CN) and analyzed by gas chromatography (GC).

Grand Canonical Monte Carlo (GCMC) Calculations.

GCMC calculations were performed in Material Studio 8.0 using "Sorption Calculation" to predict the distribution of electron density and adsorption sites of guest molecules in the skeleton. 1 × 1 × 1 unit cell was used as a model for the calculations. 1×10^6 steps were used for equilibration and 1×10^7 production steps were used to calculate the ensemble average of gas adsorption sites. The cutoff radius used for the Lennard−Jones interactions was 18.5 Å. The long-range electrostatic interactions were treated using the Ewald summation technique.

Band Gap Calculation.

The band gaps of SNNU-384 and SNNU-385 MOFs were calculated using the Tauc method based on UV-Vis spectrum, the equation is as follows:

$$(\alpha h\nu)^n = A(h\nu - E_g) \qquad \text{(eq. 3)}$$

where α is the absorption coefficient, h is Planck's constant, ν is the photon's frequency, n=2 (indirect semiconductor), Eg is the band gap, and A is the slope of the Tauc plot in the linear region.

DFT Calculation.

DFT calculations were performed with Gaussian 16 at the B3LYP/6-311G(d,p) level. The $TPHAP^0$ and $TPHAP^{1-}$ forms of TPHAP were geometrically optimized, with frequency calculations confirming true energetic minima. Frontier molecular orbital energy levels, nitrogen dp orbital contributions, and ESP maps were derived from optimized structures, with ESP maps visualized using GaussView 6.0.

Table S1. Crystal data and structure refinements for SNNU-384 and SNNU-385.

MOF	**SNNU-384**	**SNNU-385**
Formula	$C_{74}H_{42}Co_3N_{18}O_{13}$	$C_{94}H_{55}N_{15}Ni_3O_{12}$
Formula weight	1570.087	2895.24
Temperature (K)	153.00	200.00
Crystal system	trigonal	trigonal
Space group	*R*-3*c*	*R*-3
a (Å)	31.2160(13)	30.0610
b (Å)	31.2160(13)	30.0610
c (Å)	62.980(4)	38.7580
α (°)	90	90
β (°)	90	90
γ (°)	120	120
V (Å^3)	53148.0(6)	30331.6(17)
Z	18	6
ρ_{calc} (g/cm^3)	1.323	0.951
μ (mm^{-1})	0.495	0.333
F(000)	22122.0	9168.0
GOF	1.093	0.979
R_{int}	0.1952	0.0981
[a]R_1, wR^2 [I>2δ(I)]	0.1089 0.2846	0.0562 0.1636
[a]R_1, wR^2 [all data]	0.1717 0.3246	0.0890 0.1829
Largest diff. peak/hole (e Å^{-3})	0.74/-0.47	0.45/-0.34
CCDC number	2527749	2527750

[a]$R_1 = \sum(|F_o|-|F_c|)/\sum|F_o|$, $wR_2 = [\sum\omega(F_o^2–F_c^2)^2/\sum w(F_o^2)^2]^{0.5}$

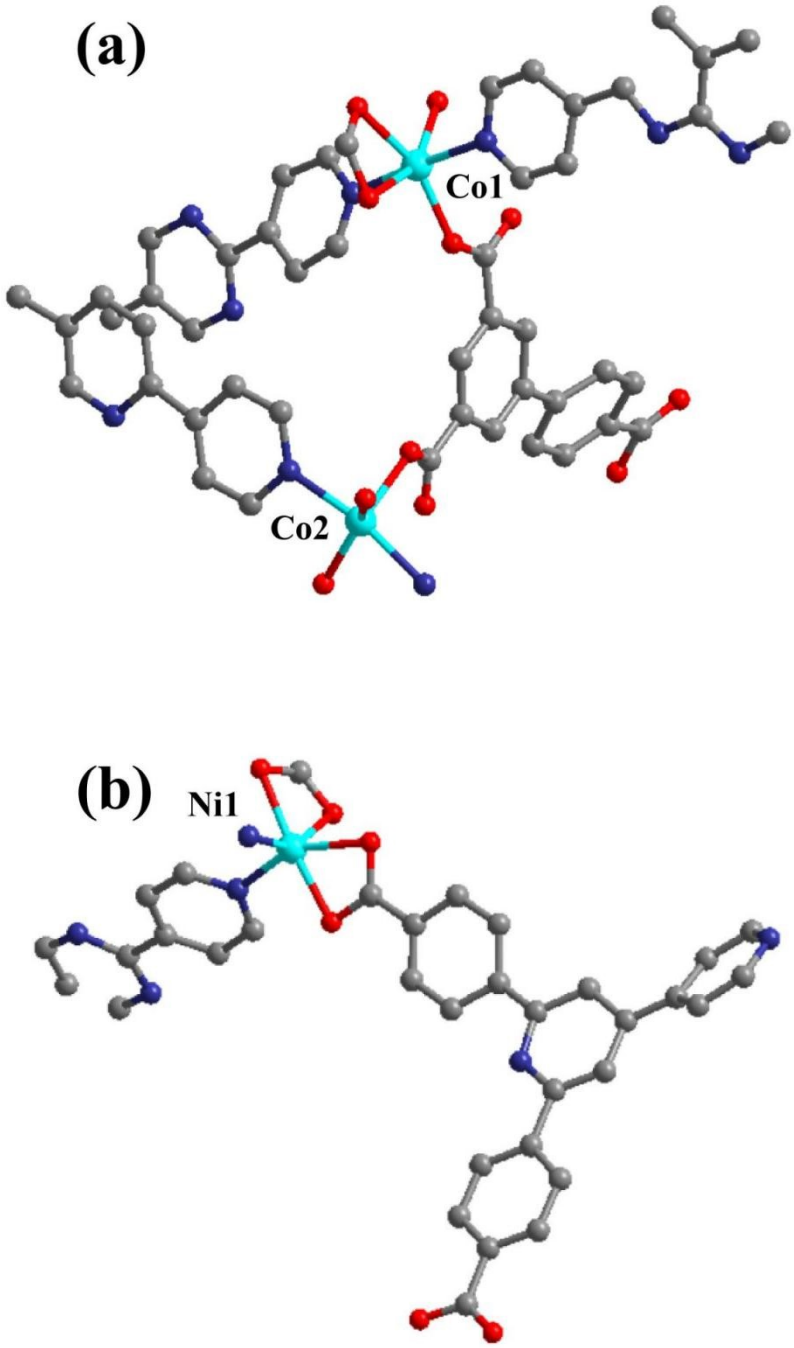

Figure S1. Asymmetric units of SNNU-384 (a) and SNNU-385 (b).

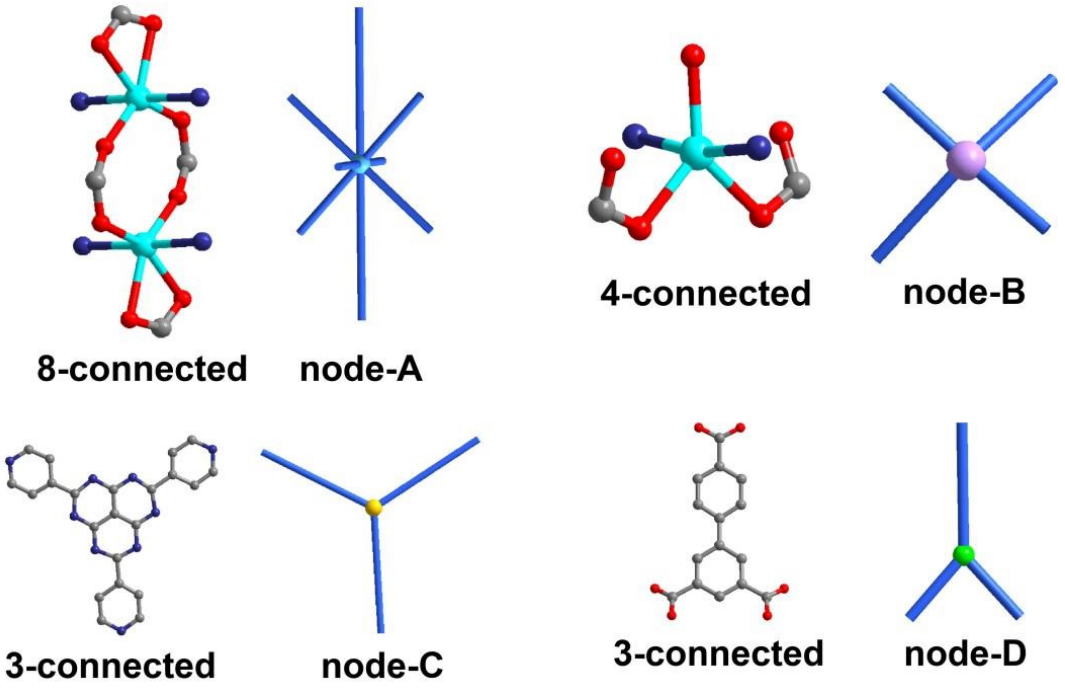

Figure S2 Simplified topological nodes (8-/4-/3-connected nodes A/B/C/D) for SNNU-384.

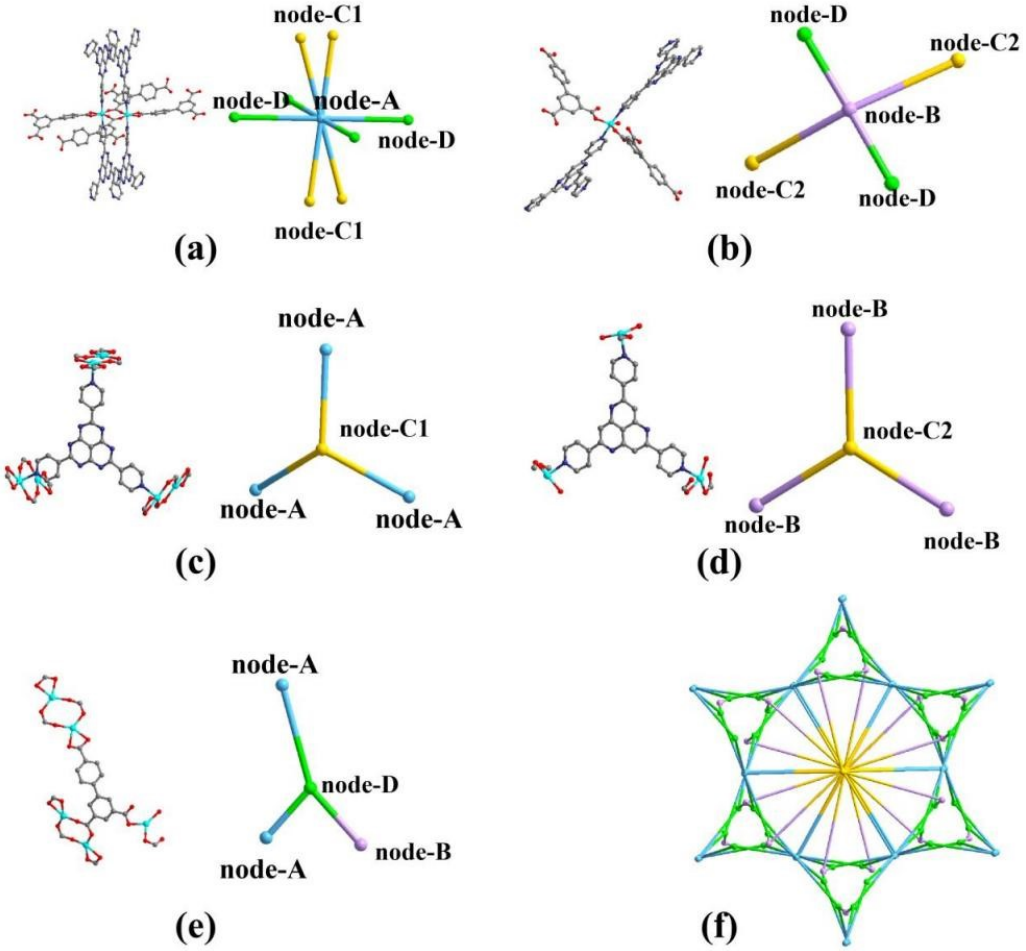

Figure S3. Coordination environments (a–e) and topological representation (f) for SNNU-384.

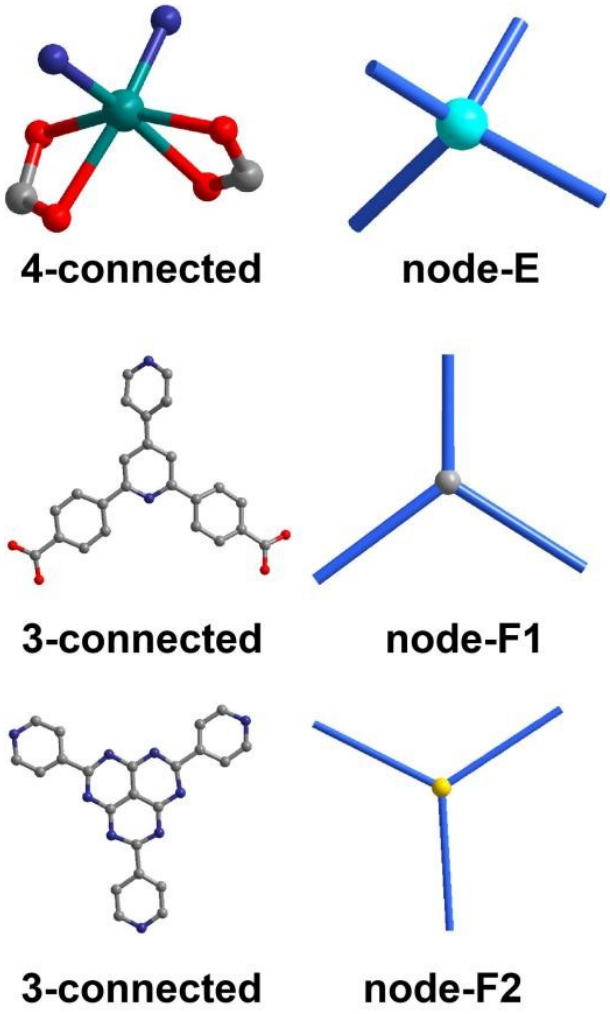

Figure S4. Simplified topological nodes (4-connected node-E, 3-connected nodes F1/F2) for SNNU-385.

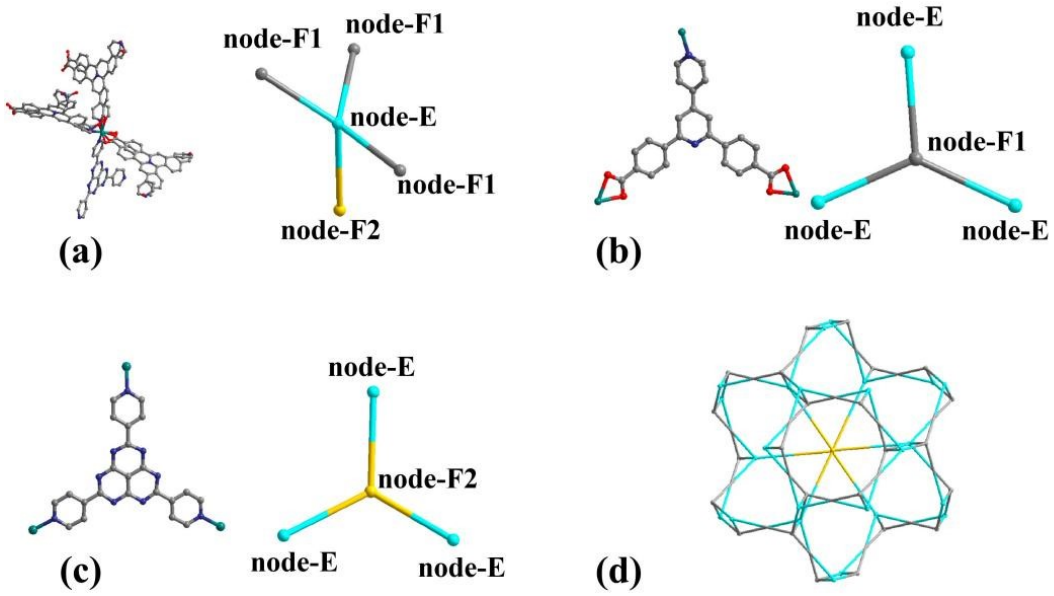

Figure S5. Coordination environments (a-c) and topological representation (d) for SNNU-385.

Table S2. The fitting parameters of virial model and the corresponding correlation coefficients of SNNU-384 and SNNU-385.

MOF	SNNU-384	SNNU-385
a0	-3516.12989	-3255.90331
a1	255.60063	1010.57019
a2	412.7444	129.87976
a3	-653.97429	-302.17889
a4	392.15858	-25.20941
a5	-133.84722	192.74568
a6	26.26476	-125.14049
a7	-2.75787	34.03956
a8	0.12	-3.478
b0	16.37262	17.92746
b1	-1.4742	19.65205
b2	0.53402	-10.54088
R^2	0.99792	0.97954

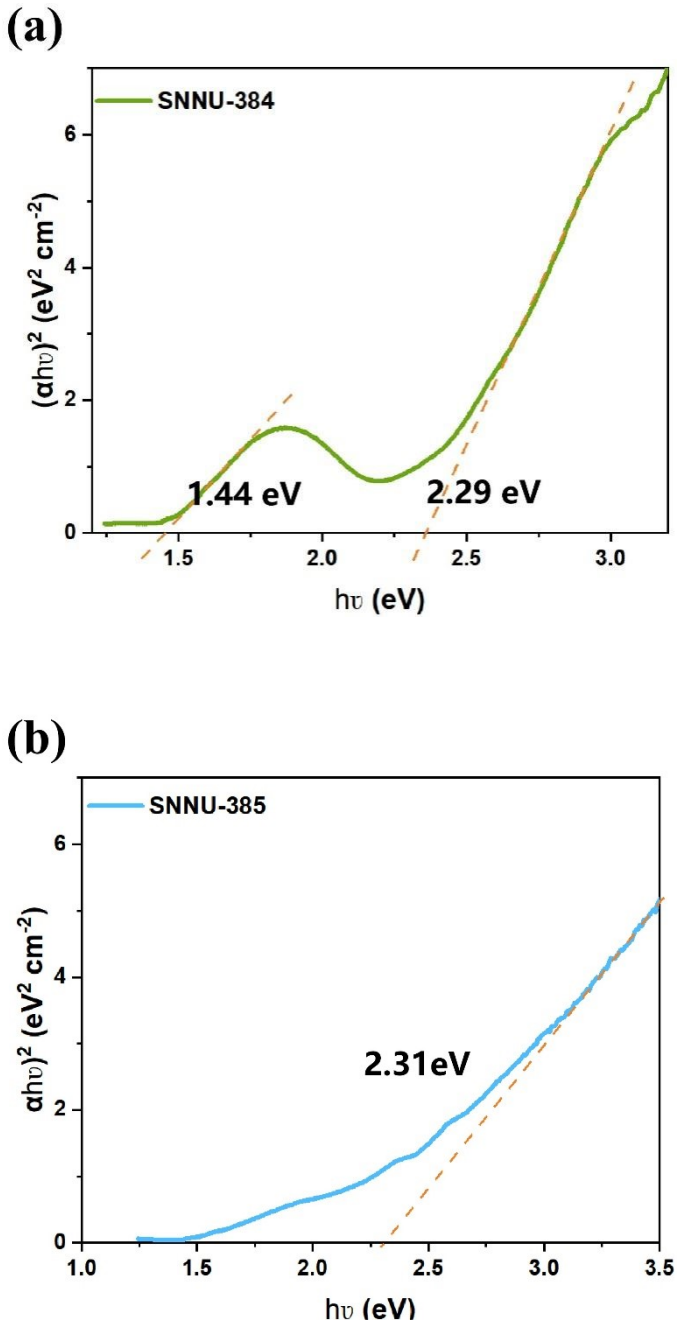

Figure S6. Band gap determination by Tauc plot for SNNU-384 and SNNU-385.

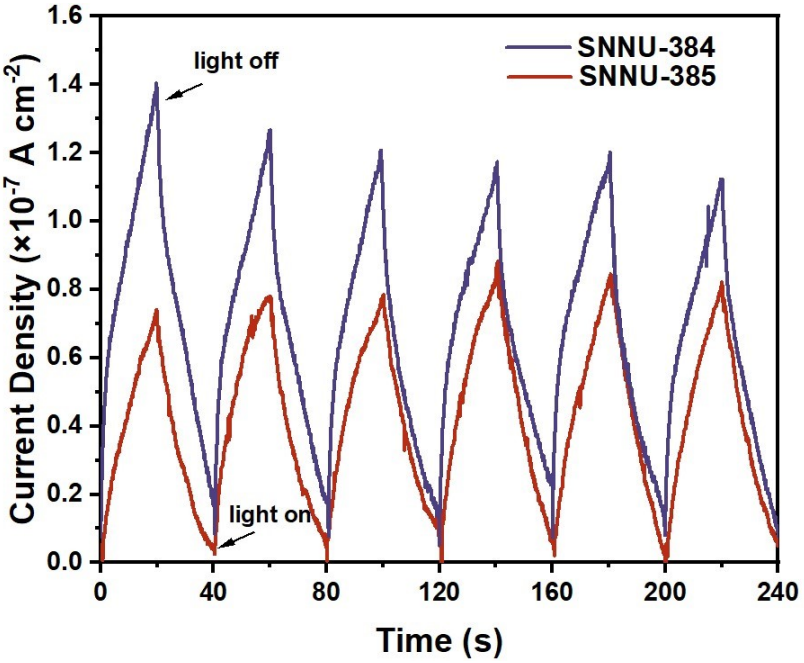

Figure S7. Transient photocurrent responses of SNNU-384 and SNNU-385.

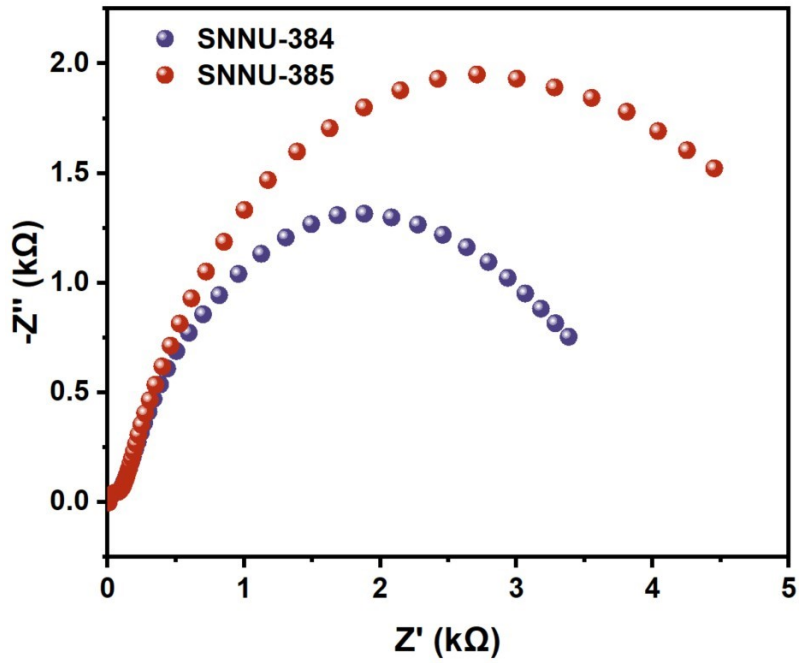

Figure S8. Electrochemical impedance spectroscopy Nyquist plots of SNNU-384 and SNNU-385.

Table S3. The porosity of SNNU-384 and SNNU-385.

MOF	N_2 uptake at 77 K and 1 bar ($cm^3\ g^{-1}$)	BET surface Area ($m^2\ g^{-1}$)	pore volume ($cm^3\ g^{-1}$)	pore width (nm)
SNNU-384	374.3	1034.8	0.57	0.56
SNNU-385	115.2	292.1	0.16	0.72

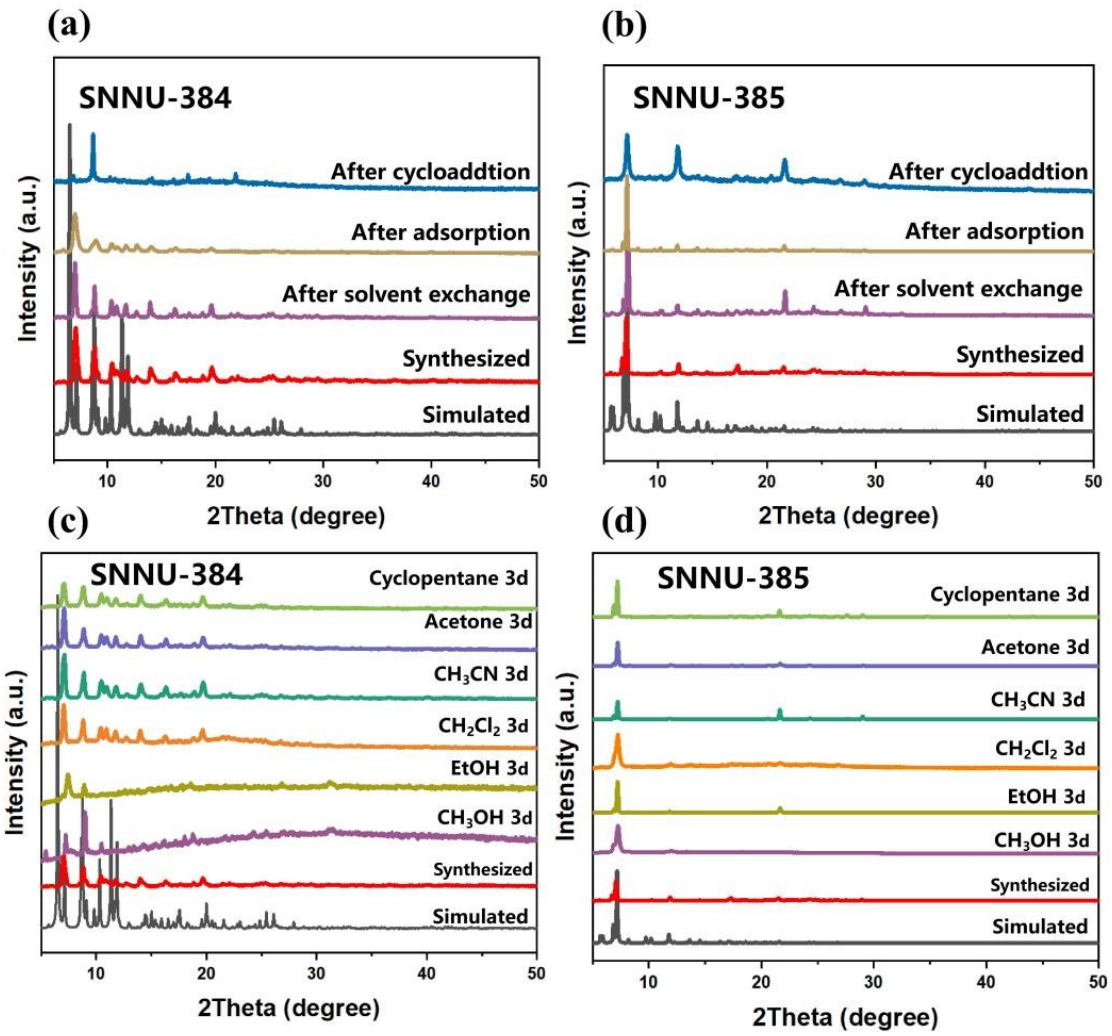

Figure S9. PXRD patterns of SNNU-384/385: post-treatment (a, b) and after stability evaluation (c, d).

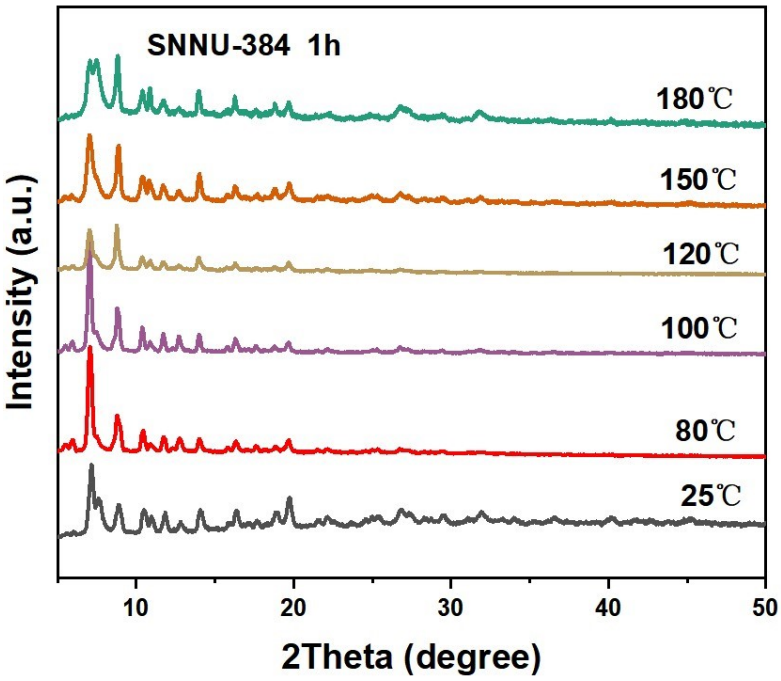

Figure S10. PXRD patterns of SNNU-384 after thermal stability evaluation.

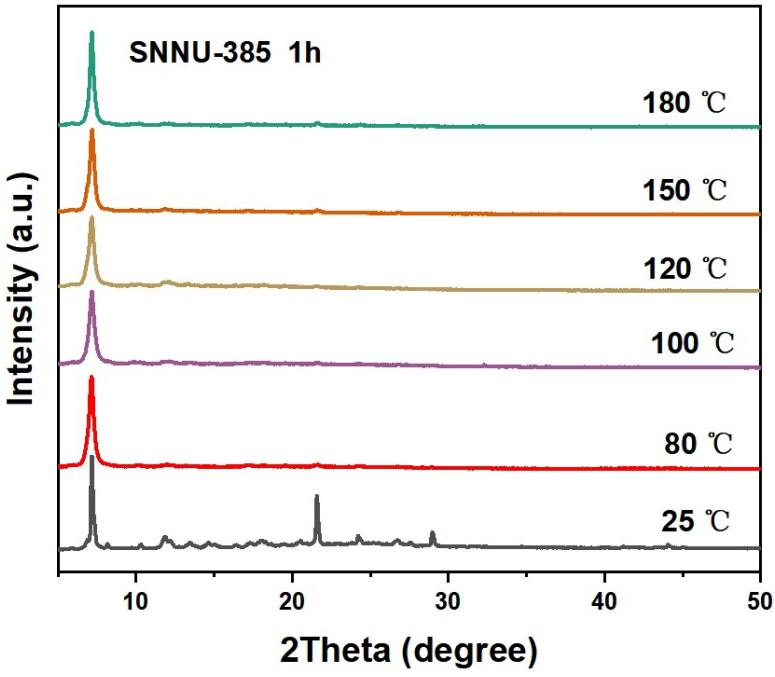

Figure S11. PXRD patterns of SNNU-385 after thermal stability evaluation.

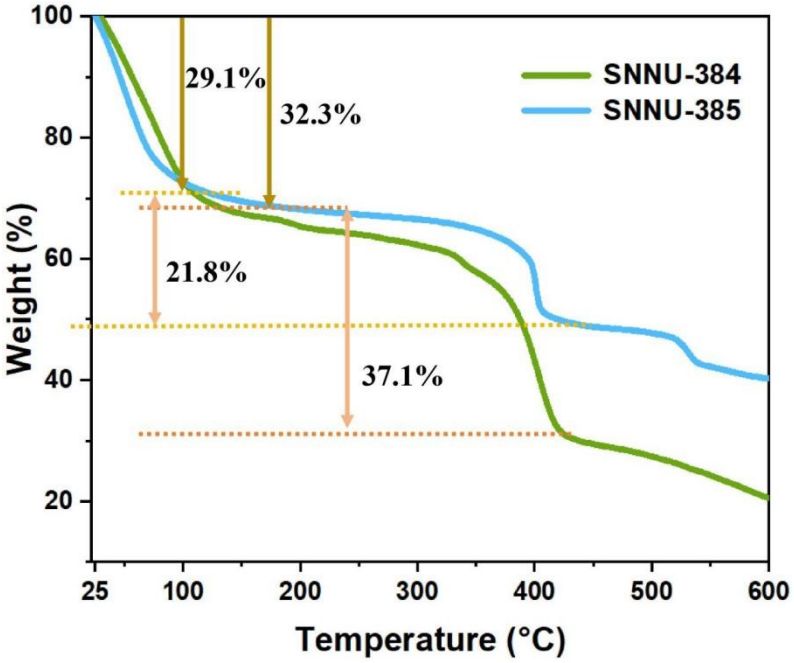

Figure S12. TGA curves of SNNU-384 and SNNU-385.

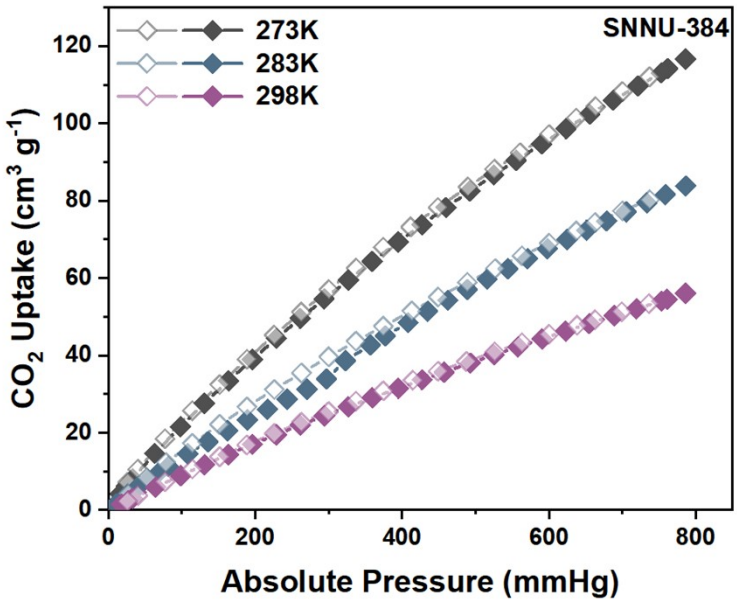

Figure S13. Fitted CO_2 adsorption isotherms of SNNU-384 measured at 273, 283, and 298 K.

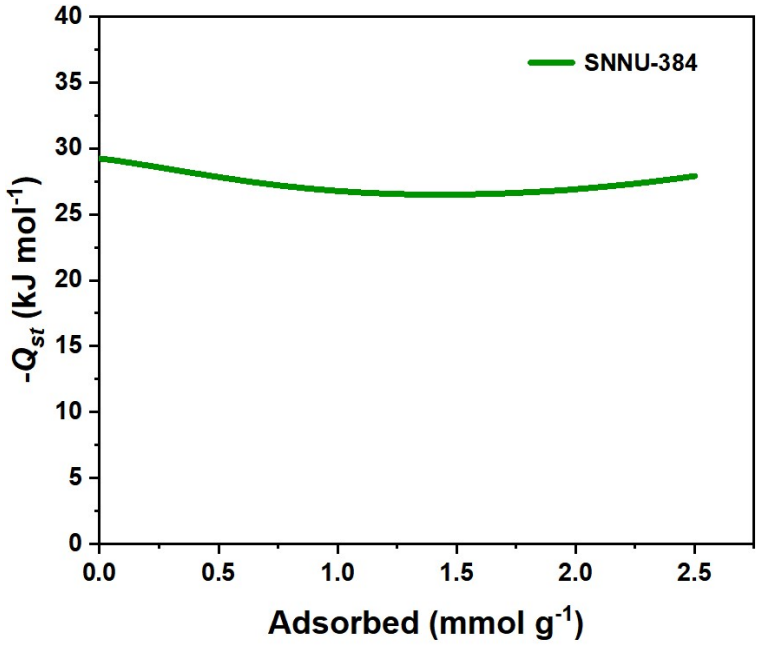

Figure S14 The isosteric heats of CO_2 adsorption for SNNU-384.

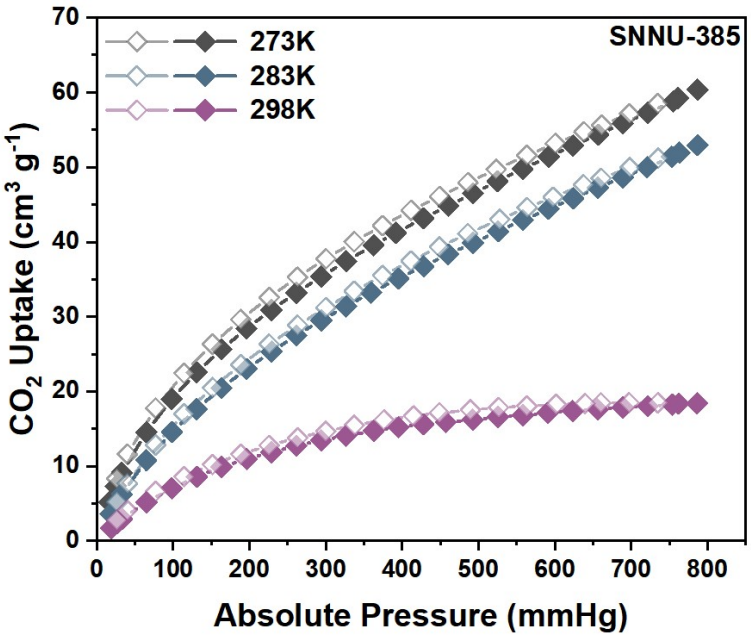

Figure S15. Fitted CO_2 adsorption isotherms of SNNU-385 measured at 273, 283, and 298 K.

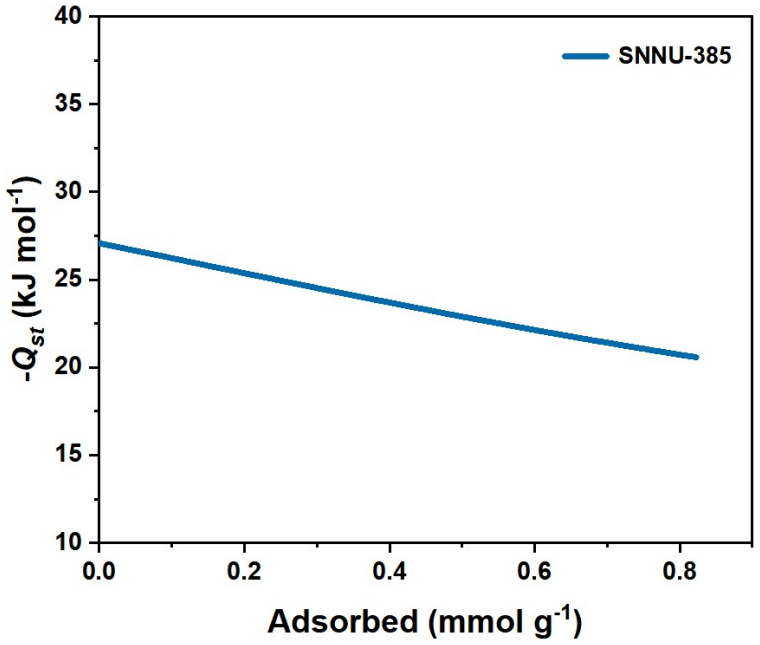

Figure S16. The isosteric heats of CO_2 adsorption for SNNU-385.

Table S4. The photocatalytic cycloaddition of CO_2 with different epoxides by SNNU-384 and SNNU-385.[a]

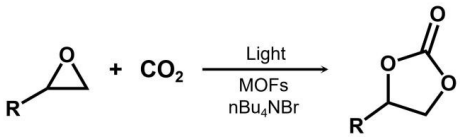

Entry	catalyst	Pressure (bar)	Co-Catalyst	Epoxide	Yield [b] (%)	Selectivity [b] (%)	TOF [c] (h^{-1})
1	SNNU-384	1	nBu_4NBr		63.0	>99	65.96
2	SNNU-385	1	nBu_4NBr		12.8	>99	14.06
3[d]	SNNU-384	1	—		13	—	—
4[e]	—	1	nBu_4NBr		5	—	—
5[f]	SNNU-384	2	nBu_4NBr		72.7	>99	76.12
6[f]	SNNU-384	4	nBu_4NBr		83.2	>99	87.1
7[f]	SNNU-384	6	nBu_4NBr		85.6	>99	89.61
8[f]	SNNU-384	8	nBu_4NBr		88.9	>99	93.00
9	SNNU-384	1	nBu_4NBr	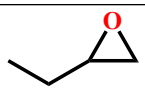	47.0	>99	49.22
10	SNNU-385	1	nBu_4NBr		27.3	>99	30
11	SNNU-384	1	nBu_4NBr	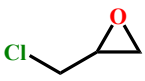	85.2	>80	89.00
12	SNNU-385	1	nBu_4NBr		60.1	>82	66.04
13	SNNU-384	1	nBu_4NBr	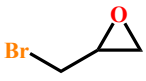	93.8	>95	98.20
14	SNNU-385	1	nBu_4NBr		72.6	>93	79.78
15	SNNU-384	1	nBu_4NBr	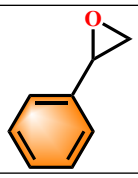	99.5	>97	104.18

16	SNNU-385	1	nBu_4NBr		99.7	＞97	109.34

[a] Reaction conditions: epoxide (20 mmol), catalyst (0.12 mol %), CO_2 (1-8 bar), and nBu_4NBr (3 mol %) under a 300 W Xe lamp for 8 h.

[b] Conversion and selectivity were determined by GC.

[c] Moles of cyclic carbonates produced per 2 moles of TPHAP active sites per hour for SNNU-384, and per mole of TPHAP active site per hour for SNNU-385.

[d] In the absence of cocatalyst nBu_4NBr.

[e] In the absence of the catalyst.

[f] Catalytic reactions under different pressure conditions.

Table S5. Comparison of typical MOFs for the conversion of CO_2 and epoxides to CCs under mild conditions. (under the visible light irradiation and use nBu_4Br)

Catalyst	Substrate	Temp. (℃)	Pressure (bar)	Time (h)	Yield (%)	TOF (h^{-1})	Ref.
SNNU-384	-CH_3	RT	1	8	63.0	65.9	This work
SNNU-384	-CH_2Cl	RT	1	8	85.2	89.0	This work
SNNU-385	-CH_2Br	RT	1	8	72.6	79.8	This work
SNNU-385	-Ph	RT	1	8	99.7	109.3	This work
Cr-MIL-101	-CH_3	RT	8[c]	24	82	10.3	S1
Hf-Vu-1000	-Ph	RT	1	56	100	-	S2
MMCF-2	-CH_3	RT	1	48	95.4	5.3	S3
MOF-505	-CH_3	RT	1	48	48.8	4	S3
HKUST-1	-CH_3	RT	1	48	49.2	4.1	S3
MMPF-9	-CH_3	RT	1	48	87.4	14.6	S4
USTC-253-TFA	-CH_3	RT	1	72	81.3	1.2	S5
UiO-67	-CH_2Cl	90[b]	1	14	98	8.09	S6
Sr-MOF	-CH_3	RT	1	48	98.5	2.4	S7
Co-tzpa-MOF	-CH_3	RT	1	48	93.8	-	S8

ZnMOF-1	$-CH_2Cl$	40[b]	1	8	99	-	S9
Sm/Gd-BTB	$-CH_3$	80[b]	1	15	100	13.07	S10
$[Mn(TCPP)_{0.5}(H_2O)_2]_n$	$-CH_3$	RT	1	24	100	8.3	S11
Co-MOF	$-CH_2Cl$	80[b]	8[c]	15	94	31.3	S12
[Ce(HTCPB)]-MOF	-Ph	100[b]	20[c]	12	98.5	20.2	S13
Ce_2NDC_3	-Ph	RT	1	8	89.0	45.0	S14
$Cd_3(TCA)_2(L)$	-Ph	RT	1	8	20	49.8	S15
Cu2(ABTC)	-Ph	50[b]	1	8	62	-	S16
$Cu_6(L)_3(H_2O)_6]\cdot(14DMF)(9H_2O)$	-Ph	RT	1	8	89	-	S17

[a] Unless otherwise stated, all data were measured under the identical conditions: room temperature, 1 bar CO_2, and visible light irradiation.

[b] This works employ higher temperatures in their catalytic systems.

[c] This works employ higher pressure in their catalytic systems.

(a)

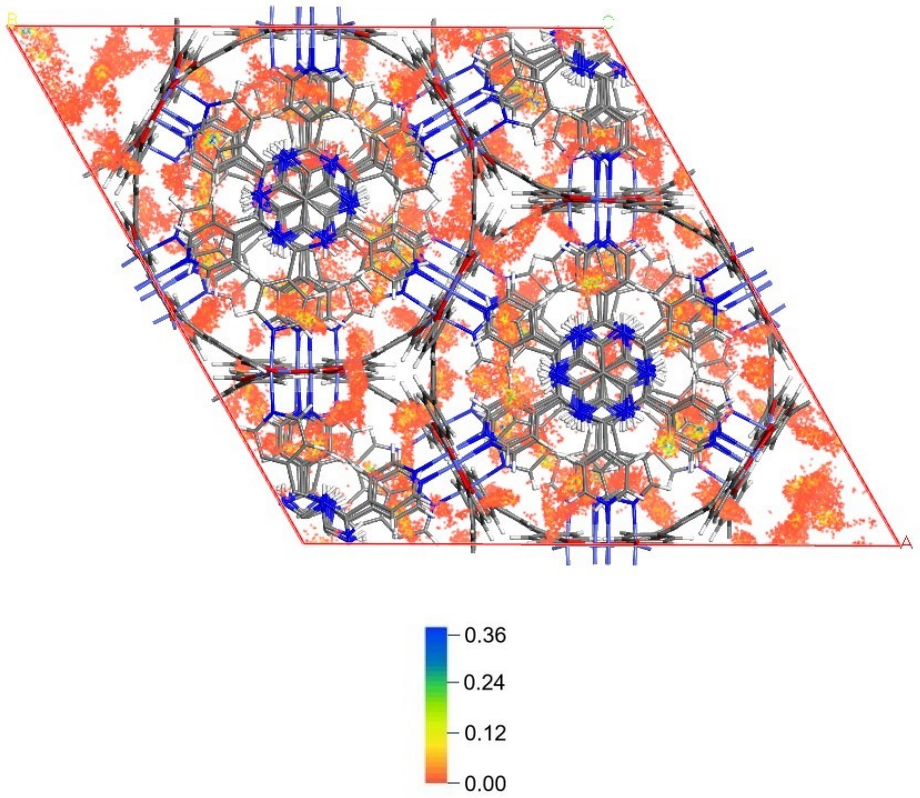

(b)

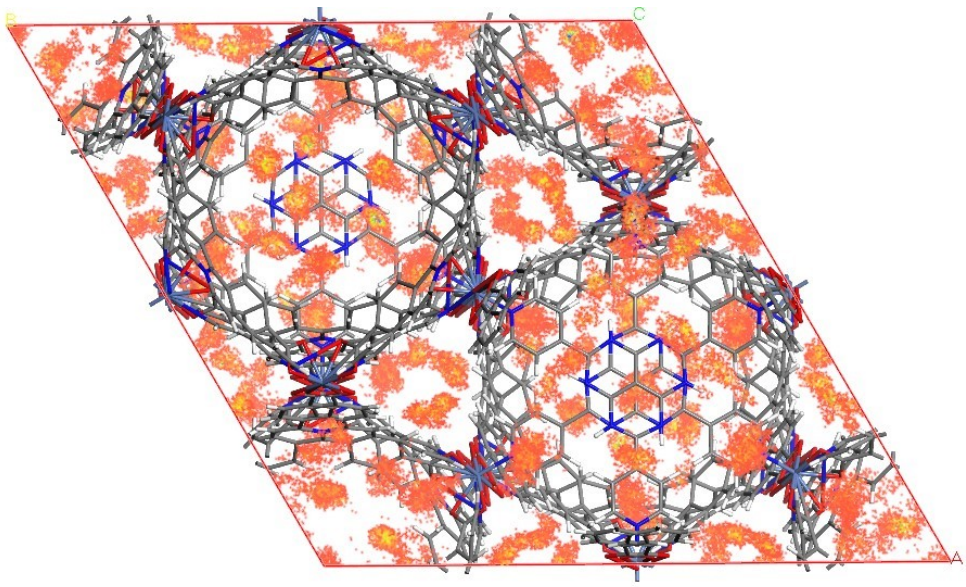

Figure S17. GCMC calculations for density distribution maps of propylene oxide in SNNU-384 (a) and SNNU-385 (b).

(a)

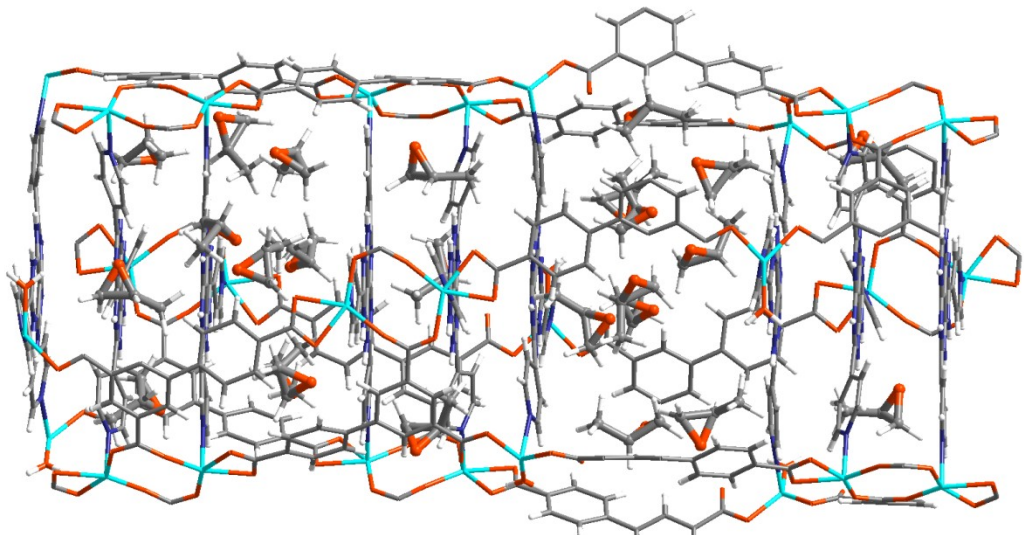

(b)

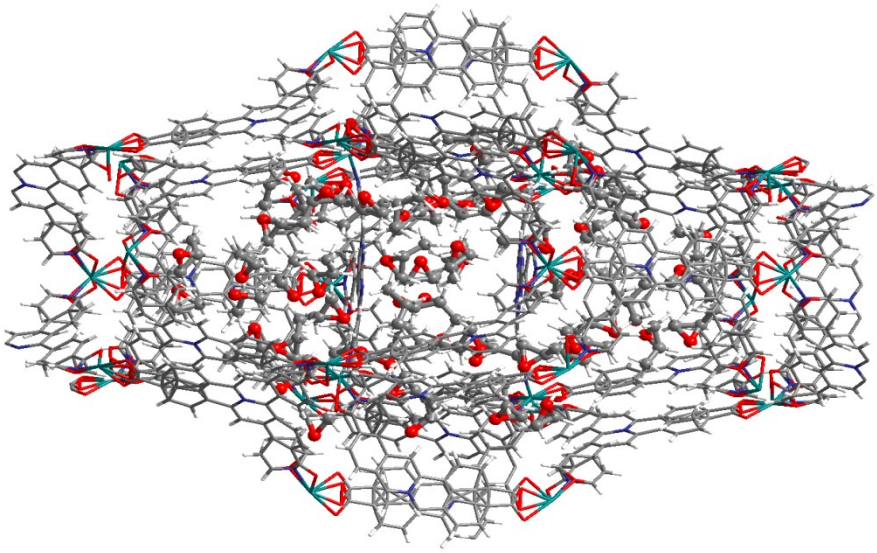

Figure S18. Binding sites and distribution of epoxides within the MOF frameworks of SNNU-384 (a) and SNNU-385 (b).

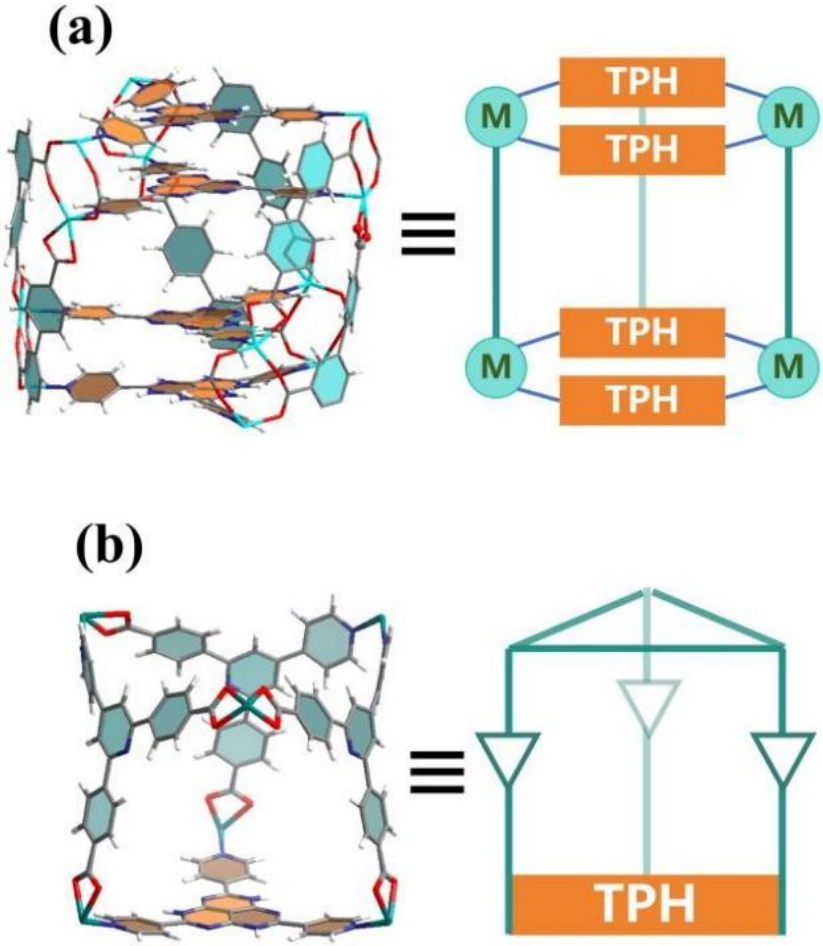

Figure S19. Simplified framework for the mechanism of SNNU-384 (a) and SNNU-385(b).

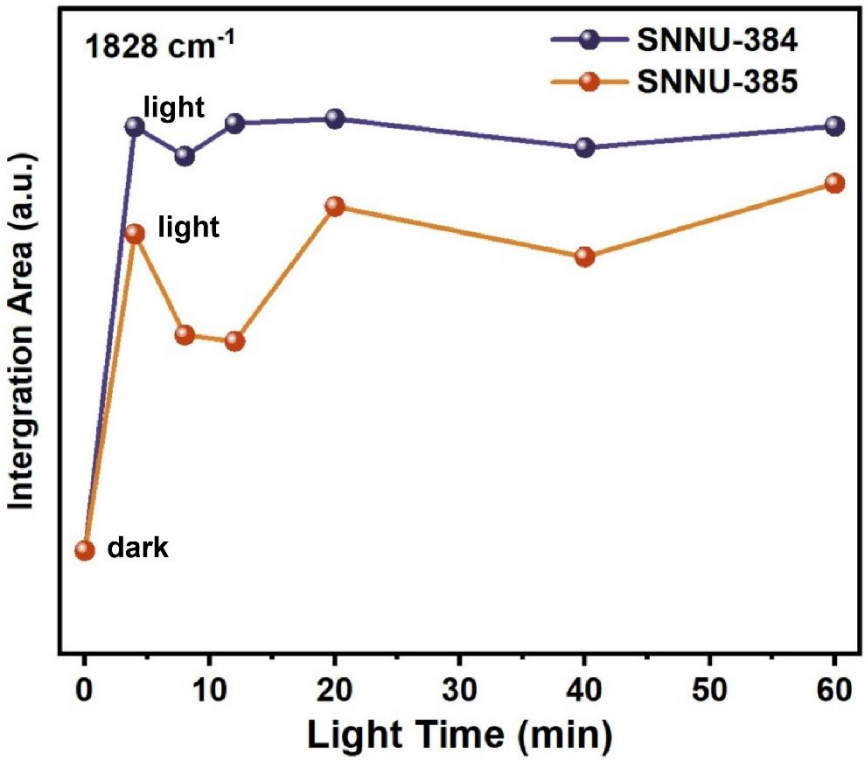

Figure S20. Comparison of the temporal evolution of carbonate intermediate (1828 cm^{-1}) over SNNU-384 and SNNU-385 monitored by in-situ FT-IR spectroscopy.

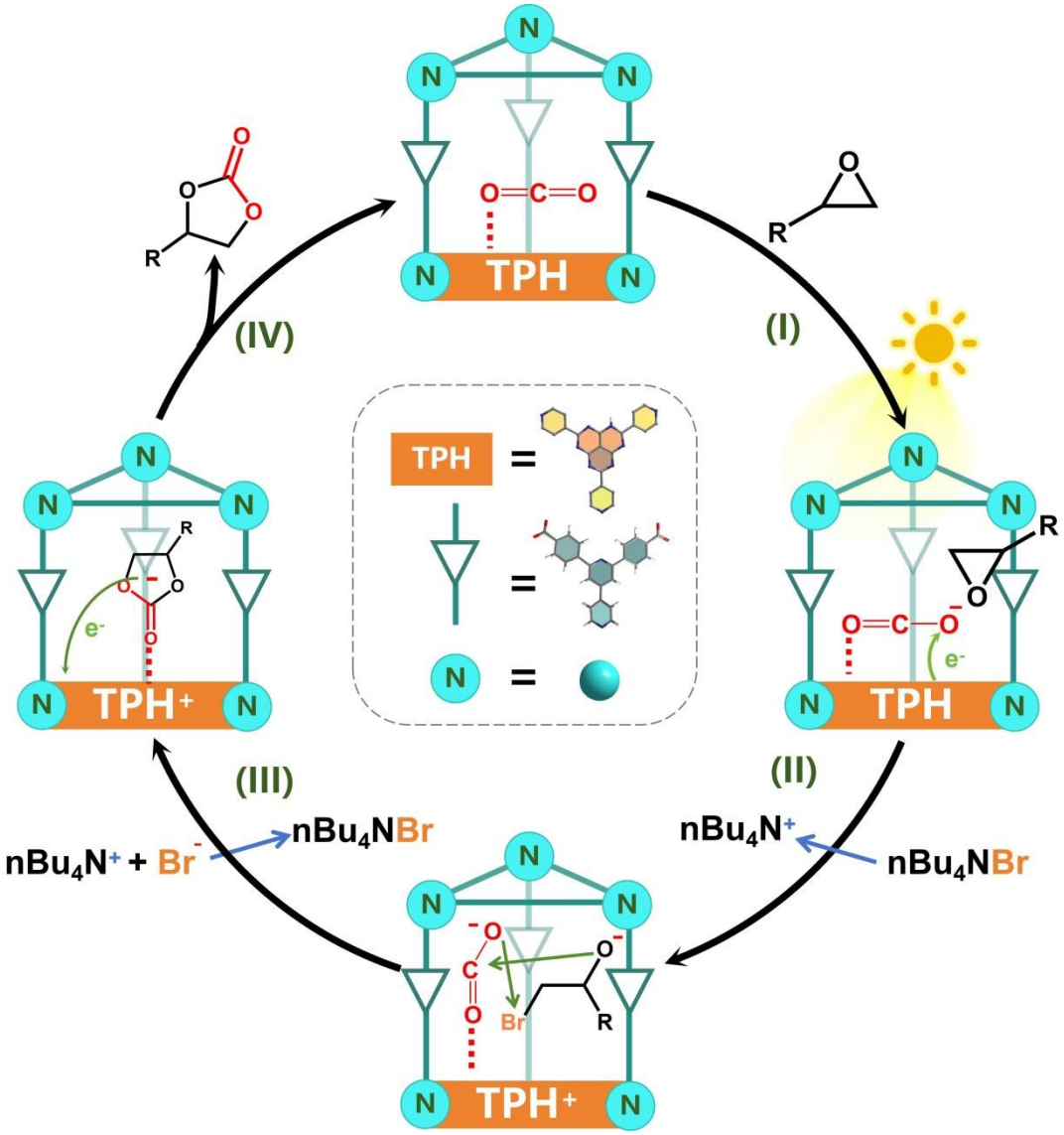

Figure S21. Reaction mechanism for the photocatalytic conversion of epoxides into CCs over SNNU-385.

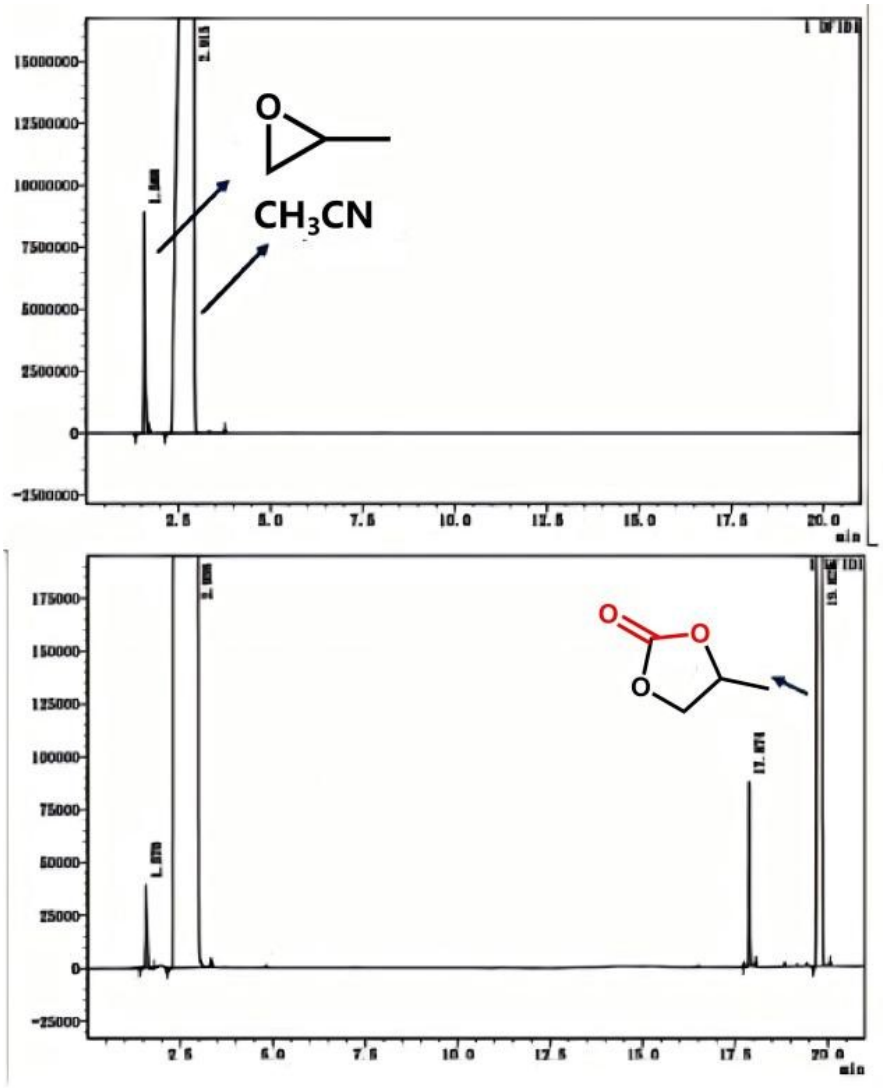

Figure S22. Gas chromatography (GC) characterization of epoxides and the products (2-methyloxirane and 4-methyl-1,3-dioxolan-2-one).

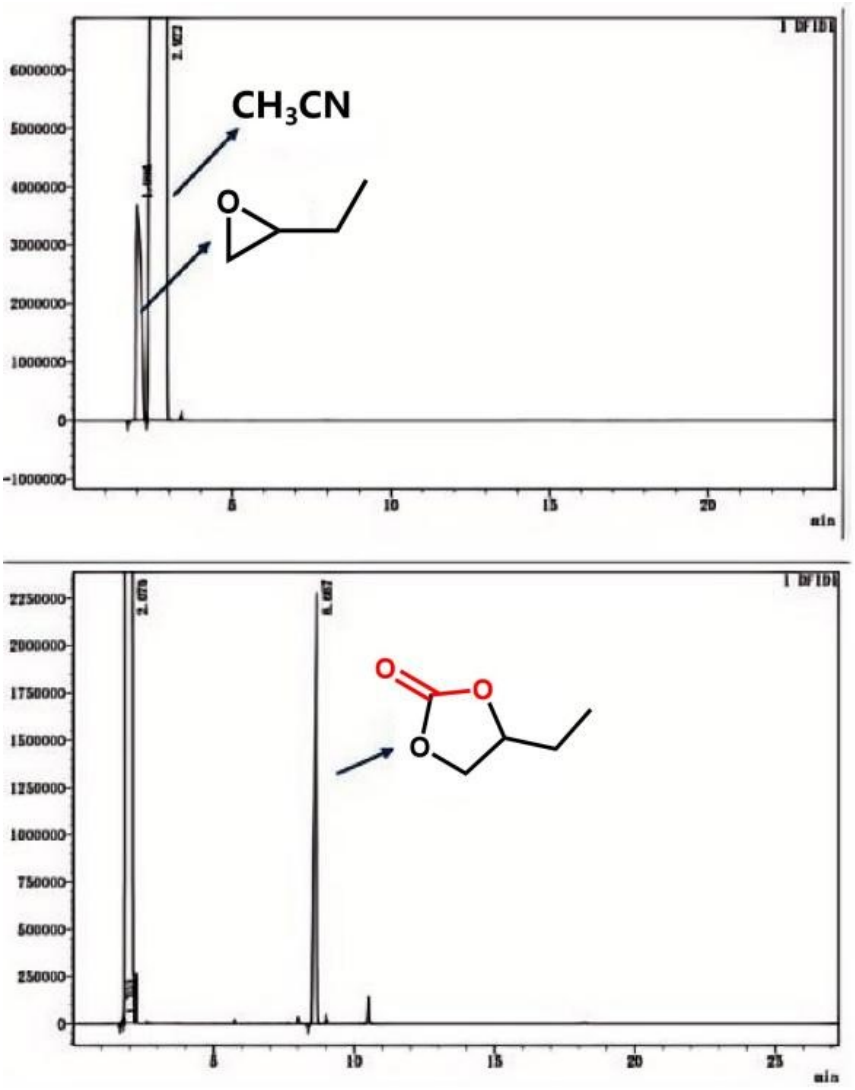

Figure S23. Gas chromatography (GC) characterization of epoxides and the products (2-ethyloxirane and 4-ethyl-1,3-dioxolan-2-one).

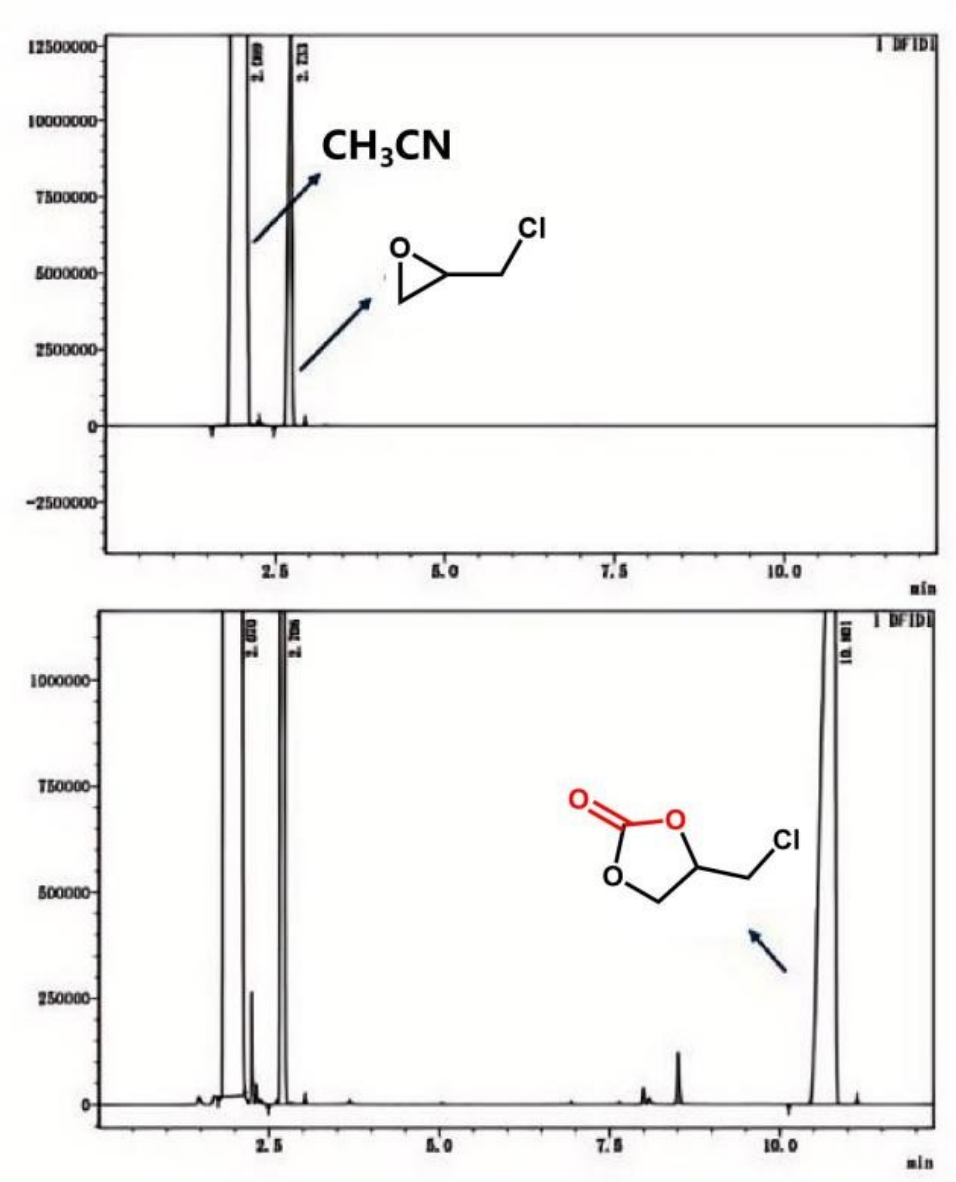

Figure S24. Gas chromatography (GC) characterization of epoxides and the products (2-(chloromethyl)oxirane and 4-(chloromethyl)-1,3-dioxolan-2-one).

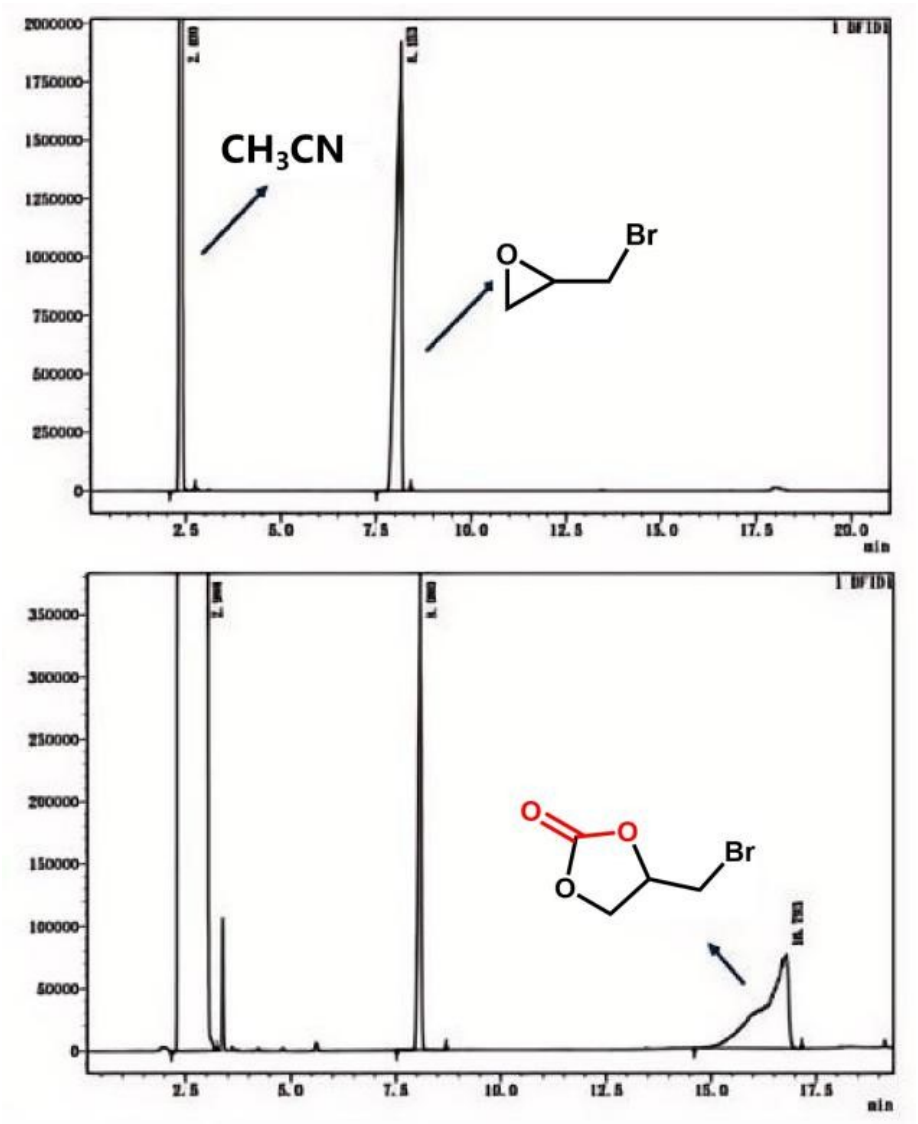

Figure S25. Gas chromatography (GC) characterization of epoxides and the products (2-(bromomethyl)oxirane and 4-(bromomethyl)-1,3-dioxolan-2-one).

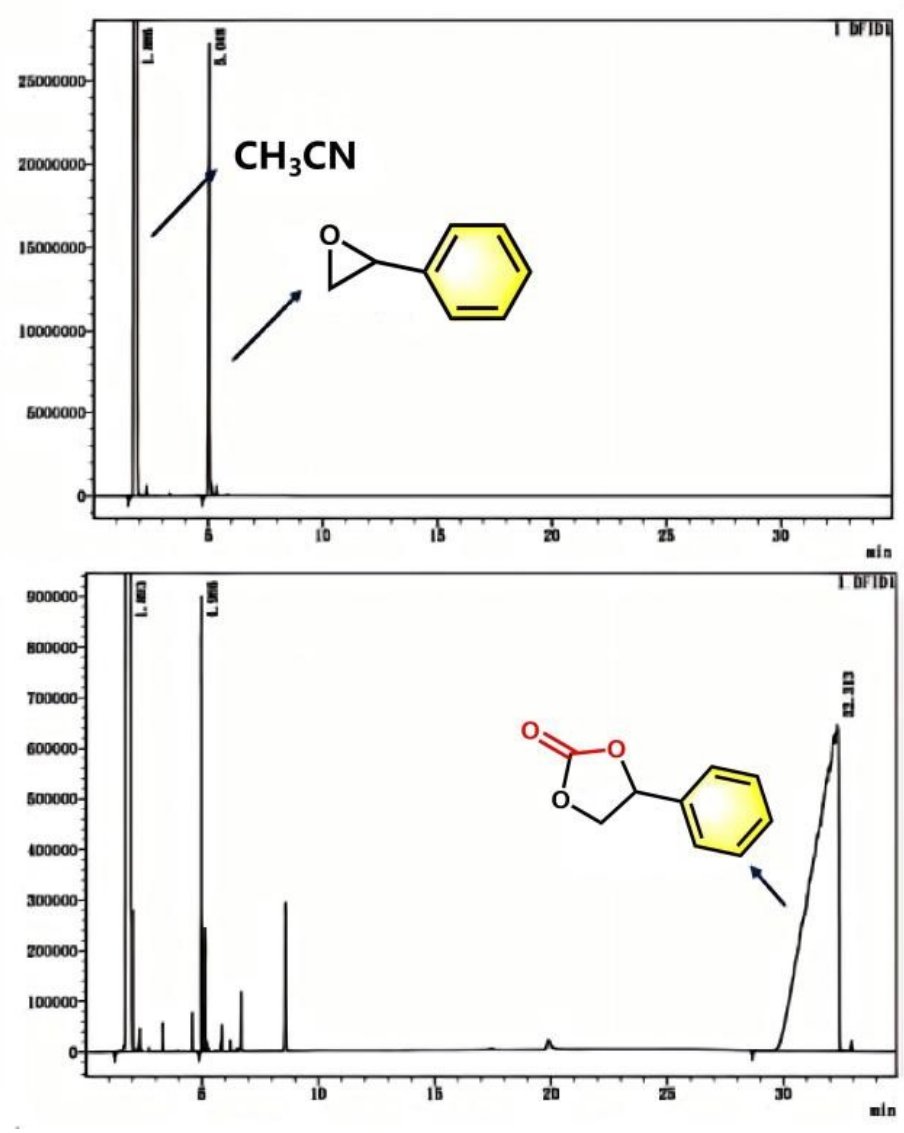

Figure S26. Gas chromatography (GC) characterization of epoxides and the products (2-phenyloxirane and 4-phenyl-1,3-dioxolan-2-one).

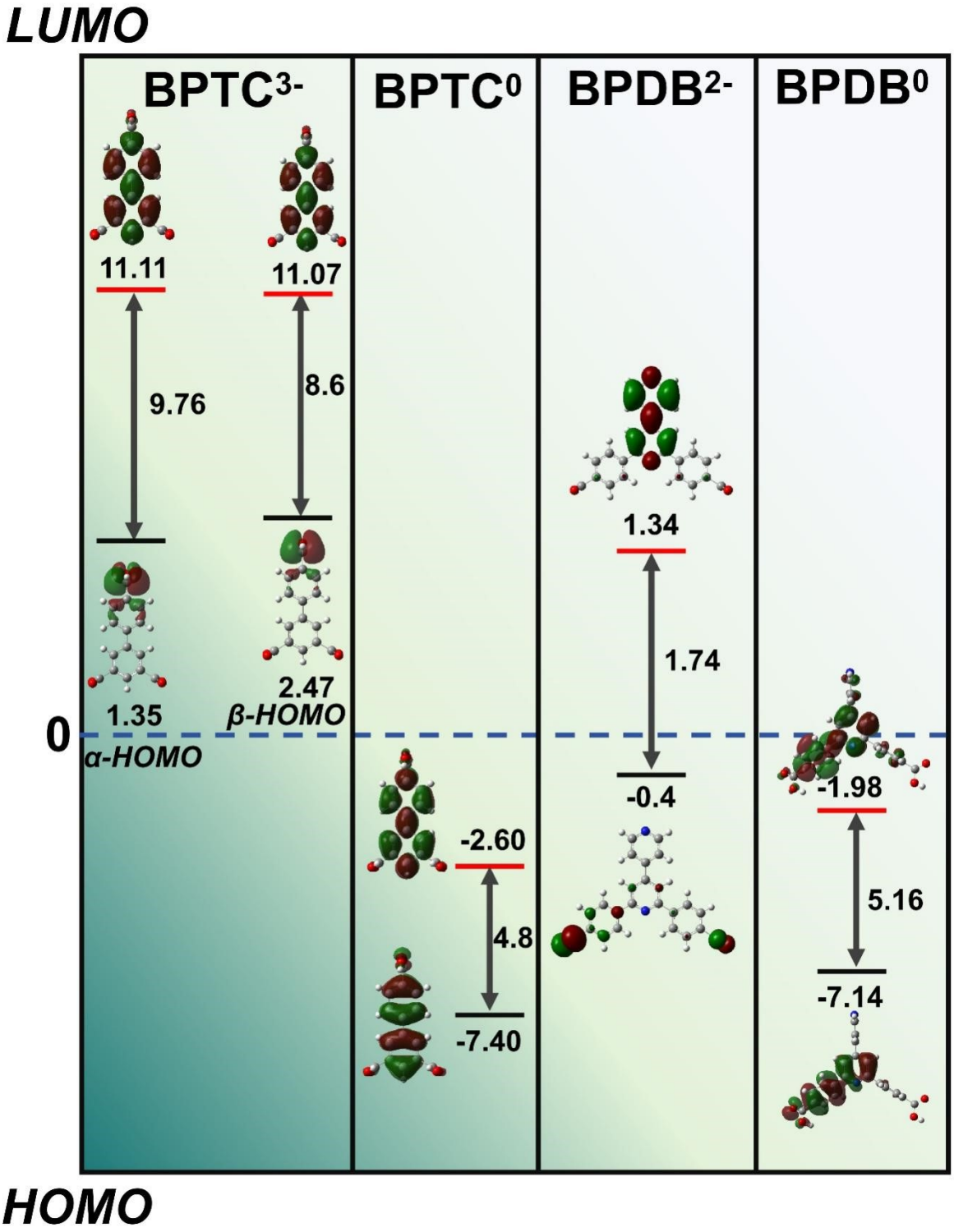

Figure S27. The calculated HOMO-LUMO information of corresponding ligands in different valence states.

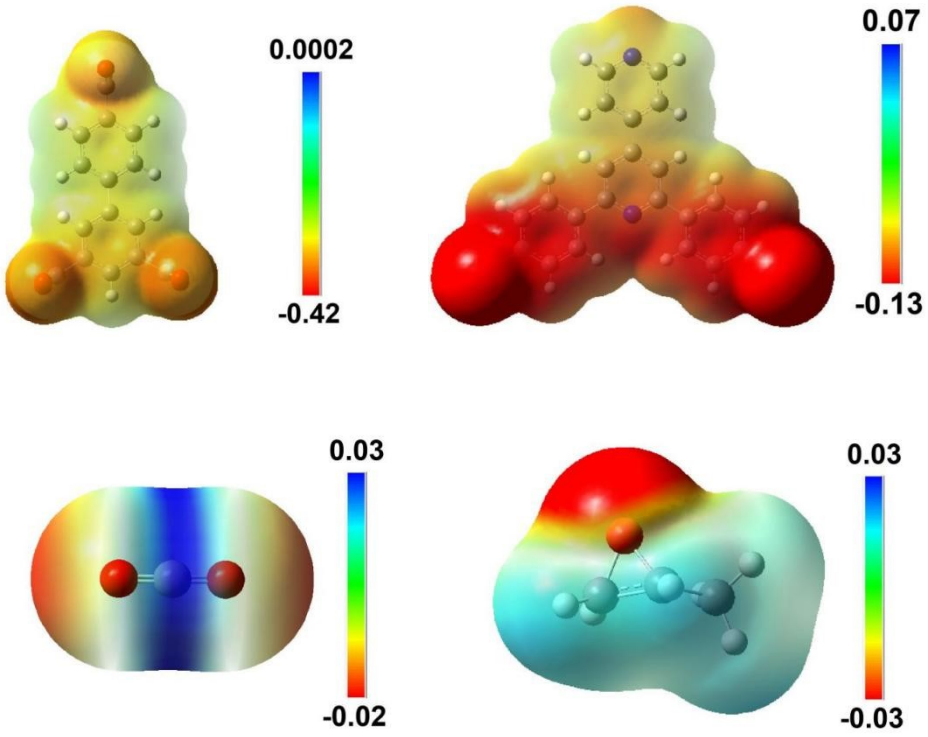

Figure S28. The calculated ESP data for BPTC, BPDB, CO_2 and PO.

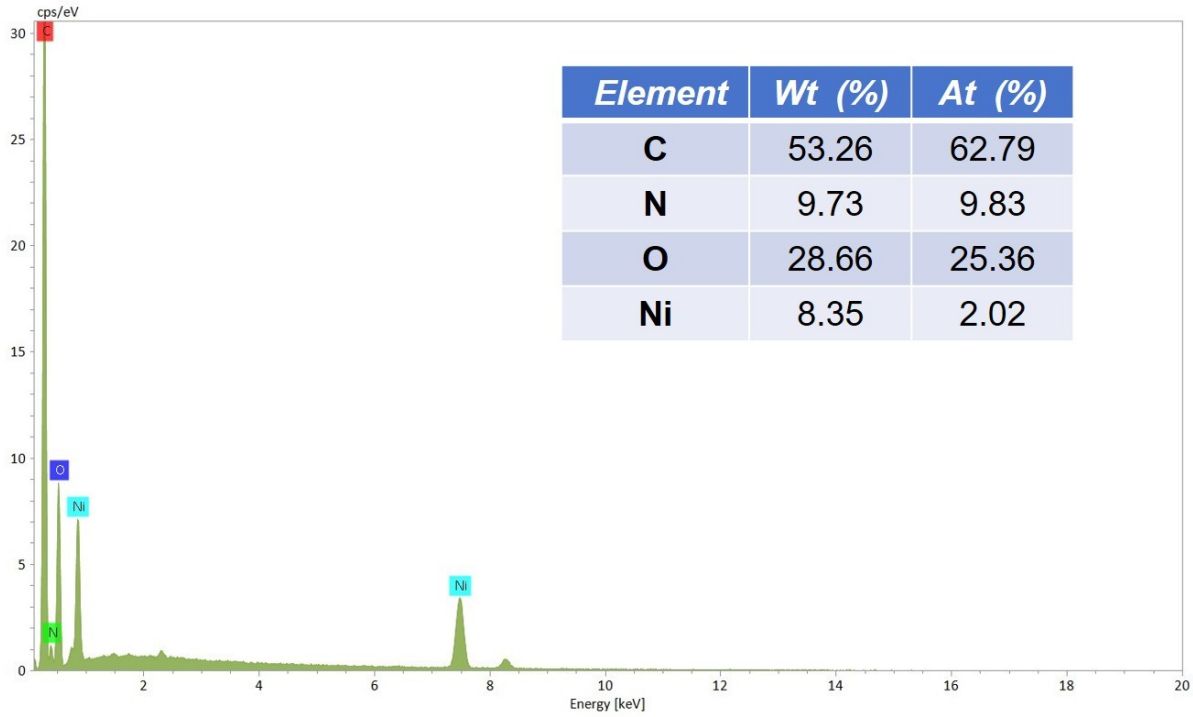

Element	Wt (%)	At (%)
C	53.26	62.79
N	9.73	9.83
O	28.66	25.36
Ni	8.35	2.02

Figure S29. The EDS results of SNNU-384.

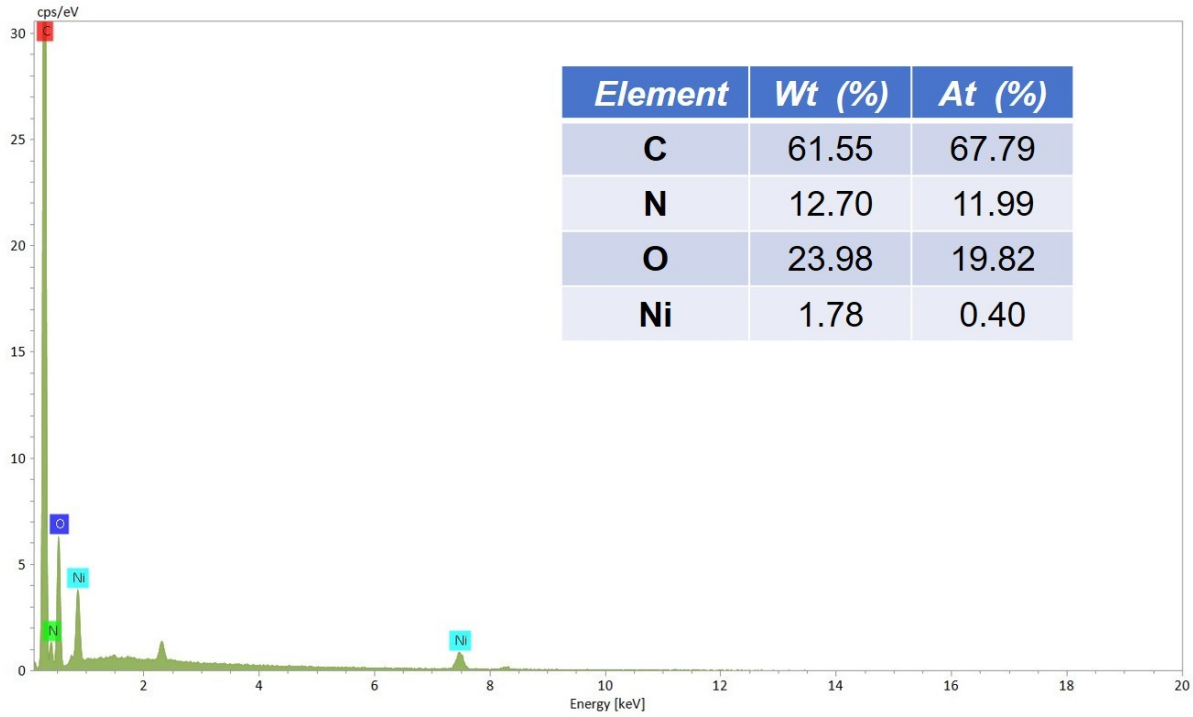

Element	Wt (%)	At (%)
C	61.55	67.79
N	12.70	11.99
O	23.98	19.82
Ni	1.78	0.40

Figure S30. The EDS results of SNNU-385.

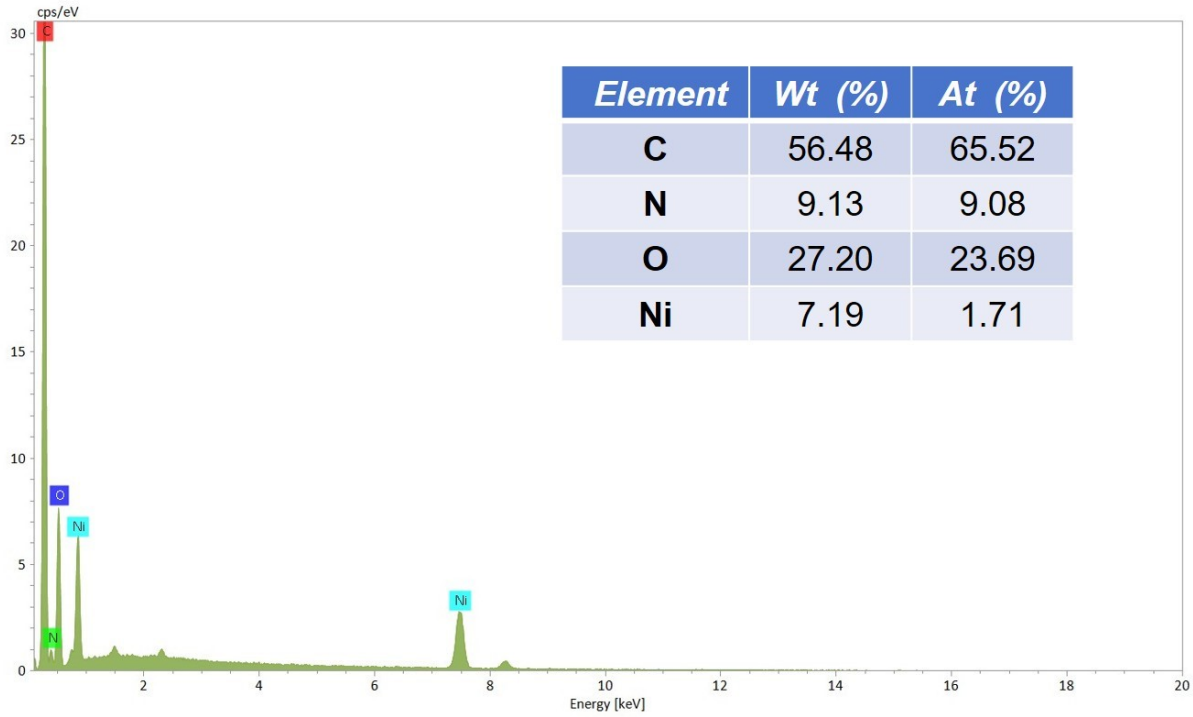

Element	Wt (%)	At (%)
C	56.48	65.52
N	9.13	9.08
O	27.20	23.69
Ni	7.19	1.71

Figure S31. The EDS results of SNNU-384 after 6 cycle of catalysis.

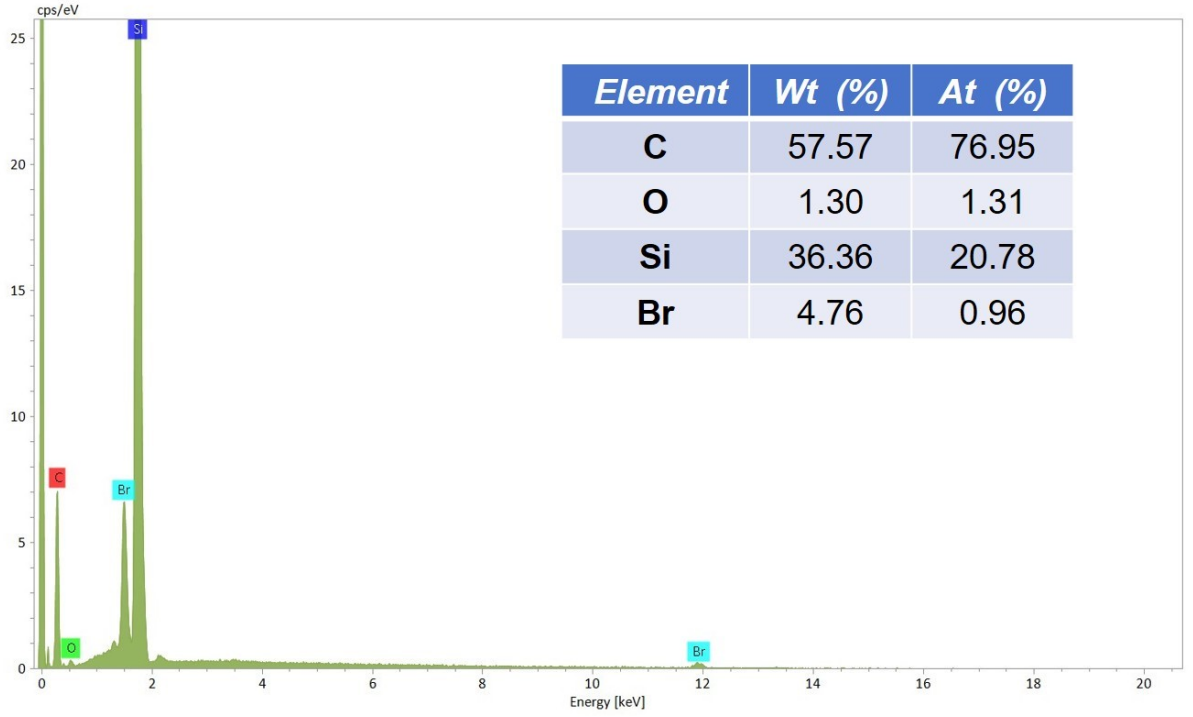

Element	Wt (%)	At (%)
C	57.57	76.95
O	1.30	1.31
Si	36.36	20.78
Br	4.76	0.96

Figure S32. The EDS results of the reaction mixture after the 6 catalytic cycles of SNNU-384.

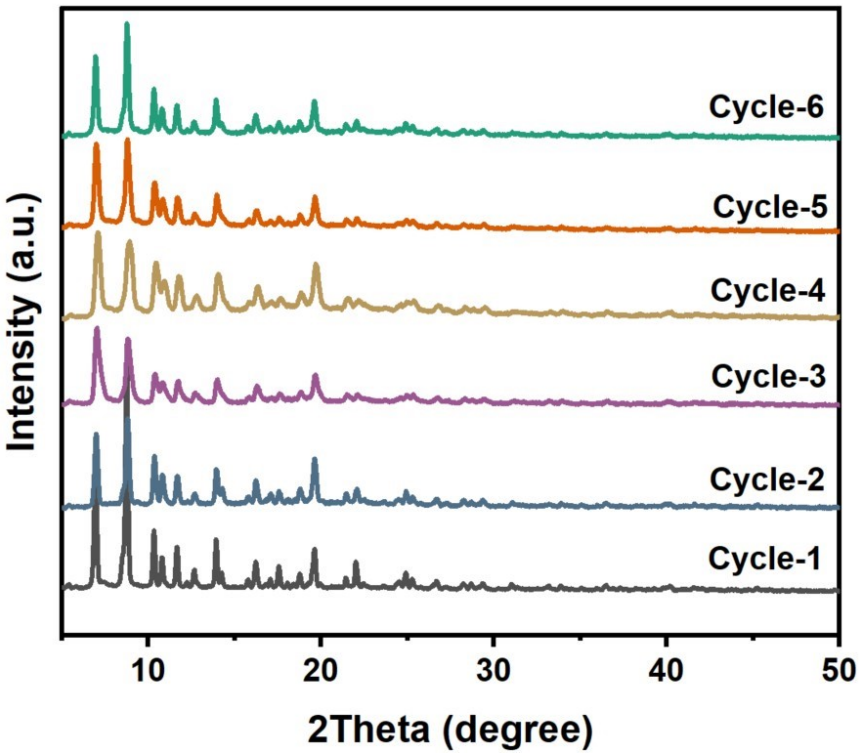

Figure S33. The PXRD of SNNU-384 after 6 cycles of catalysis.

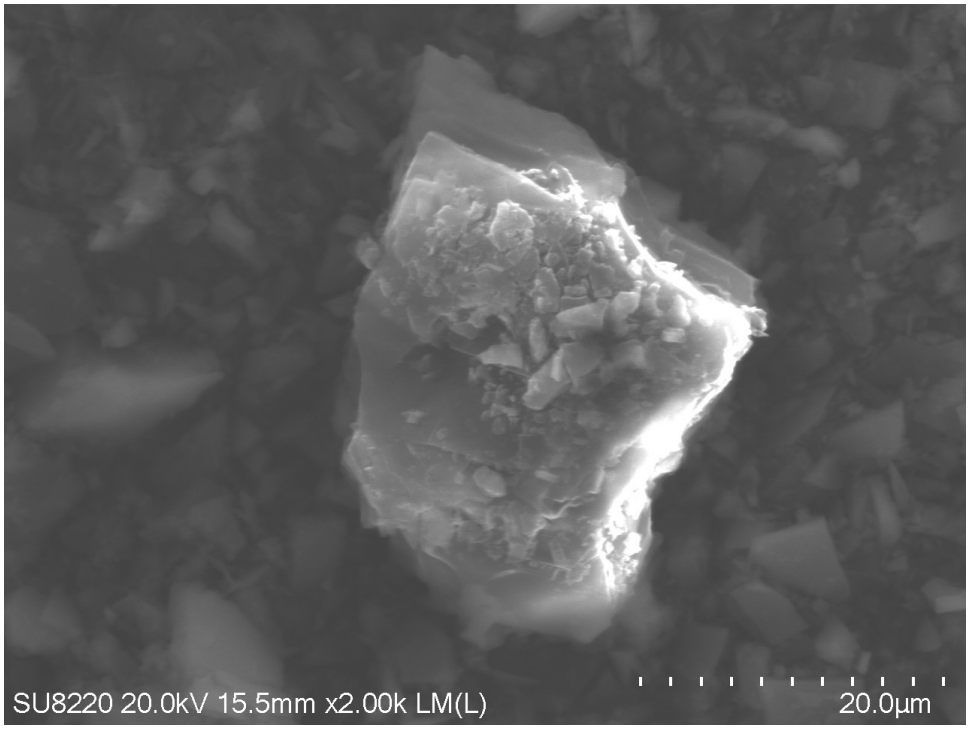

Figure S34. The SEM of SNNU-384 after 6 cycles of catalysis.

Reference

(S1) O. V. Zalomaeva, A. M. Chibiryaev, K. A. Kovalenko, O. A. Kholdeeva, B. S. Balzhinimaev and V. P. Fedin, J. Catal., 2013, **298**, 179-185.

(S2) H. Beyzavi, R. C. Klet, S. Tussupbayev, J. Borycz, N. A. Vermeulen, C. J. Cramer, J. F. Stoddart, J. T. Hupp and O. K. Farha, J. Am. Chem. Soc., 2014, **136**, 15861-15864.

(S3) W.-Y. Gao, Y. Chen, Y. Niu, K. Williams, L. Cash, P. J. Perez, L. Wojtas, J. Cai, Y.-S. Chen and S. Ma, Angew. Chem. Int. Ed., 2014, **53**, 2615-2619.

(S4) W.-Y. Gao, L. Wojtas and S. Ma, Chem. Commun., 2014, **50**, 5316-5318.

(S5) Z.-R. Jiang, H. Wang, Y. Hu, J. Lu and H. L. Jiang, ChemSusChem, 2015, **8**, 878-885.

(S6) L.-G. Ding, B.-J. Yao, W.-L. Jiang, J.-T. Li, Q.-J. Fu, Y.-A. Li, Z.-H. Liu, J. P. Ma and Y. B. Dong, Inorg. Chem, 2017, **56**, 2337-2344.

(S7) X.-Y. Li, Y.-Z. Li, Y.-Yang, L. Hou, Y.-Y. Wang and Z. Zhu, Chem. Commun., 2017, **53**, 12970-12973.

(S8) H.-H. Wang, L. Hou, Y.-Z. Li, C.-Y. Jiang, Y.-Y. Wang and Z. Zhu, ACS Appl. Mater. Interfaces, 2017, **9**, 17969-17976.

(S9) P. Patel, B. Parmar, R. I. Kureshy, N.-u. Khan and E. Suresh, ChemCatChem, 2018, **10**, 2401-2408.

(S10) B. Ugale, S. S. Dhankhar and C. M. Nagaraja, Cryst. Growth Des., 2018, **18**, 2432-2440.

(S11) N. Sharma, S. S. Dhankhar and C. M. Nagaraja, Microporous Mesoporous Mater., 2019, **280**, 372-378.

(S12) B. Ugale, S. Kumar, T. J. Dhilip Kumar and C. M. Nagaraja, Inorg. Chem., 2019, **58**, 3925-3936.

(S13) D.-H. Le, R. P. Loughan, A. G adysiak, N. Rampal, I. A. Brooks, A.-H. A. Park, D. Fairen-Jimenez and K. C. Stylianou, J. Mater. Chem. A, 2022, **10**, 1442-1450.

(S14) S. K. Das, S. Chatterjee, S. Bhunia, A. Mondal, P. Mitra, V. Kumari, A. Pradhan and A. Bhaumik, Dalton Trans., 2017, **46**, 13783-13792.

(S15) M. Singh, P. P. Mondal, S. Rajput and S. Neogi, Inorg. Chem. Front., 2023, **10**, 3605-

3620.

(S16) P. T. K. Nguyen and Y. B. N. Tran, ChemistrySelect, 2021, **6**, 4067-4073.

(S17) V. Sharma, R. Das, R. Saha, D. De and P. K. Bharadwaj, Chem. Commun., 2017, **53**, 13371-13374.